ARTICLE

Ultrafast Charge Transfer and Recombination Dynamics in Monolayer–Multilayer WSe$_2$ Junctions Revealed by Time-Resolved Photoemission Electron Microscopy

Ce Xu, Natalie Barden, Evgeny M. Alexeev, Xiaoli Wang, Run Long, Alisson R. Cadore, Ioannis Paradisanos, Anna K. Ott, Giancarlo Soavi, Sefaattin Tongay, Giulio Cerullo, Andrea C. Ferrari,* Oleg V. Prezhdo,* and Zhi-Heng Loh*

Cite This: ACS Nano 2024, 18, 1931−1947 · Read Online

ACCESS | Metrics & More | Article Recommendations | SI Supporting Information

ABSTRACT: The ultrafast carrier dynamics of junctions between two chemically identical, but electronically distinct, transition metal dichalcogenides (TMDs) remains largely unknown. Here, we employ time-resolved photoemission electron microscopy (TR-PEEM) to probe the ultrafast carrier dynamics of a monolayer-to-multilayer (1L-ML) WSe$_2$ junction. The TR-PEEM signals recorded for the individual components of the junction reveal the sub-ps carrier cooling dynamics of 1L- and 7L-WSe$_2$, as well as few-ps exciton−exciton annihilation occurring on 1L-WSe$_2$. We observe ultrafast interfacial hole (h) transfer from 1L- to 7L-WSe$_2$ on an ∼0.2 ps time scale. The resultant excess h density in 7L-WSe$_2$ decays by carrier recombination across the junction interface on an ∼100 ps time scale. Reminiscent of the behavior at a depletion region, the TR-PEEM image reveals the h density accumulation on the 7L-WSe$_2$ interface, with a decay length ∼0.60 ± 0.17 μm. These charge transfer and recombination dynamics are in agreement with *ab initio* quantum dynamics. The computed orbital densities reveal that charge transfer occurs from the basal plane, which extends over both 1L and ML regions, to the upper plane localized on the ML region. This mode of charge transfer is distinctive to chemically homogeneous junctions of layered materials and constitutes an additional carrier deactivation pathway that should be considered in studies of 1L-TMDs found alongside their ML, a common occurrence in exfoliated samples.

KEYWORDS: transition metal dichalcogenides, lateral junction, interfacial charge transfer, time-resolved photoemission electron microscopy, ultrafast spectroscopy, nonadiabatic ab initio molecular dynamics
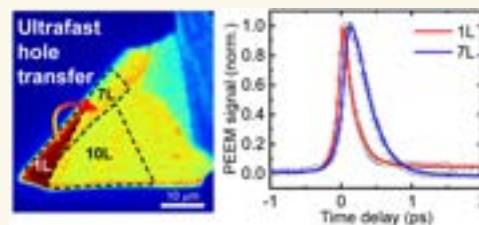
L ayered materials (LMs) are at the center of an ever-expanding research effort.[1−7] Numerous electronic[1−5] and optoelectronic[1,3,6,7] properties have been uncovered in semiconducting transition metal dichalcogenides (TMDs), such as layer-sensitive electronic structures,[8−10] high carrier mobilities (∼10^1−10^3 cm^2 V$^{−1}$ s$^{−1}$),[11−13] superconductivity,[14,15] large exciton binding energies (hundreds of meV),[16−19] nonlinear optical response ($\chi^{(2)} \sim 10^{−12}$ m V$^{−1}$, $\chi^{(3)} \sim 10^{−17}$−$10^{−19}$ m^2 V$^{−2}$),[20−24] and optical properties dominated by excitonic transitions.[16−19,25−29] Along with the ability to fabricate TMDs on a wafer scale,[30−32] these allow the realization of ultrathin nanoelectronic[5] and optoelectronic devices,[6] with diverse applications, such as transistors,[11−13] photodetectors,[7,33−35] and electroluminescent devices.[36−39]

Layered material heterostructures (LMHs) comprising two chemically distinct TMDs juxtaposed either vertically or laterally have also been prepared.[31,40] Extensive experimental[41−44] and theoretical[45] studies revealed photoresponse[7,46] and photovoltaic response,[47,48] high (>10^5) field-effect ON/OFF ratio,[49] and rectification,[50] as well as intra- and interlayer excitonic physics.[51−55] The behavior of carriers at heterojunctions is dictated by the band alignment of the two TMD components.[56−58] In the case of type-I band alignment, with valence band maximum (VBM) and conduction band minimum (CBM)
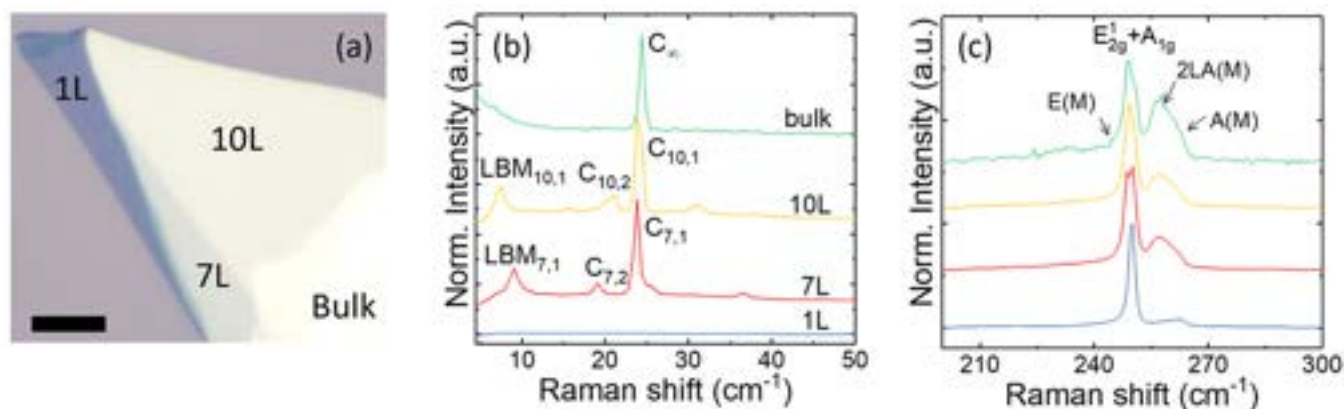
Figure 1. (a) Optical image of 1L−ML-WSe$_2$. Scale bar: 10 μm. (b) Low-frequency and (c) high-frequency Raman spectra as a function of N at 532 nm excitation.

in the same layer,[59] both electrons (e) and holes (h) transfer to the same TMD, thereby supporting applications that require radiative recombination, such as light-emitting diodes.[38] In the case of type-II band alignment, with VBM and CBM in different layers,[53] photocarriers undergo charge separation and transfer across these heterojunctions, giving rise to applications in photodetectors[7] and photovoltaics.[57,60] Investigations of type-II vertical LMHs by pump−probe spectroscopy revealed interlayer charge transfer within ∼50 fs.[61−67] Time-domain density functional theory and nonadiabatic molecular dynamics suggest that the ultrafast interlayer charge transfer is facilitated by quantum coherence and e delocalization.[68] Electronic structure calculations reveal strong interlayer coupling at the Γ valley of the valence band (VB) and the Q valley of the conduction band (CB), suggesting that these mediate interlayer charge transfer.[69] For lateral LMHs, exciton transfer across a type-I 1L-MoS$_2$−1L-MoSe$_2$ heterojunction with a velocity[70] ∼10^4 m s^{-1} and sub-ps e transfer across a type-II composition-graded 1L-WS$_2$−1L-WSe$_2$ interface were reported.[71]

TMD junctions are a complement to LMHs.[72−76] Unlike LMHs, an LM junction (LMJ) comprises the same material at the interface. However, the opposite sides of the interface exhibit distinct band gaps,[73−75] tunable by varying phase,[77] doping,[78] substrate,[79] and number of layers, N.[72,75,76,80,81] We refer to the LMJ between a single-layer (1L) and a multilayer (ML) LM as 1L−ML-LMJ. This can often be found in samples prepared by micromechanical cleavage (MC) of bulk (B)-TMDs, in which different regions correspond to different N.[72−74,80] The 1L region of a TMD 1L−ML-LMJ has a direct band gap,[82,83] whereas an indirect band gap is present in the ML region.[82,83] In the case of WSe$_2$, experimental[80,81] and theoretical[75] studies found that juxtaposing 1L-WSe$_2$, which has a direct band gap ∼1.64 eV,[84] with ML-WSe$_2$, whose indirect band gap evolves from 1.51 eV (N = 2) to 1.45 eV ($N \geq 4$),[84] yields an interface with a type-I band alignment.[75,80,81] Measurements on a 1L−3L-MoS$_2$ LMJ by scanning photocurrent microscopy suggested type-II band alignment,[72] whereas Kelvin probe force microscopy on a 1L−14L-MoS$_2$ LMJ pointed to type-I band alignment.[85]

Compared to the extensive ultrafast spectroscopy studies performed to date on TMD LMHs,[61−67,70,71] the ultrafast dynamics of 1L−ML-LMJs is, to the best of our knowledge, hitherto unexplored, mainly due to the need to combine sub-100 fs temporal and sub-100 nm spatial resolution to study the dynamics at the interface. The typical μm-scale sizes of MC-

TMDs[86] implies similar dimensions for 1L−ML-LMJs, therefore the need for an ultrafast spectroscopy technique that can simultaneously allow μm to sub-μm resolution. Time-resolved photoemission electron microscopy (TR-PEEM) is complementary to ultrafast optical microscopy[87−89] for investigating spatially resolved ultrafast phenomena. It can resolve the dynamics of trap states in B-semiconductors[71] and perovskite thin films,[90,91] image e motion in B-semiconductors[92] and LMHs,[93] and reveal spatially heterogeneous ultrafast dynamics of TMDs.[94,95]

Here, we use TR-PEEM to investigate the ultrafast e and h dynamics of a 1L−7L WSe$_2$ type-I LMJ. In addition to sub-ps carrier relaxation dynamics within the individual components, we observe an ∼0.2 ps h transfer, followed by ∼100 ps charge recombination, across the LMJ. We use nonadiabatic *ab Initio* molecular dynamics to calculate the time constants for h transfer and charge recombination, in agreement with experiments. Analysis of the PEEM images reveals the width of the depletion region at the 1L−7L-WSe$_2$ interface.

RESULTS AND DISCUSSION

The LMJ is prepared as follows. B-WSe$_2$ crystals are grown by the flux zone method.[16] These are exfoliated by MC on Nitto Denko tape,[86] then again on a polydimethylsiloxane (PDMS)[96] stamp placed on a glass slide for inspection under an optical microscope. Optical contrast[97] is optimized to identify 1L and 1L−7L-WSe$_2$ prior to transfer. The samples are then placed on 90 nm-SiO$_2$/Si at 40 °C using *xyz* micromanipulators under an optical microscope, before increasing the temperature to 60 °C, so that they detach from PDMS and adhere preferably to SiO$_2$.[96]

Figure 1a reveals regions of different N within the same flake. To characterize and identify N, we perform Raman spectroscopy and atomic force microscopy (AFM). Raman measurements are done with a Horiba LabRam Evolution system equipped with 1800 l/mm grating and volume Bragg filters with a cutoff frequency ∼5 cm^{-1} at 532 nm, with a 100× objective (numerical aperture, NA = 0.9), resulting in a spot size ∼1 μm. AFM measurements are performed with a Bruker Dimension Icon in tapping mode.

Figure 1b plots the low-frequency (<50 cm^{-1}) Raman spectra of the different regions of a WSe$_2$ flake and of B-WSe$_2$. The Raman modes in this frequency range originate from relative motion of the layers and consequently are absent in 1L-WSe$_2$.[98−102] The shear modes (C) are due to the relative motions of the planes perpendicular to their normal,[98−102] while
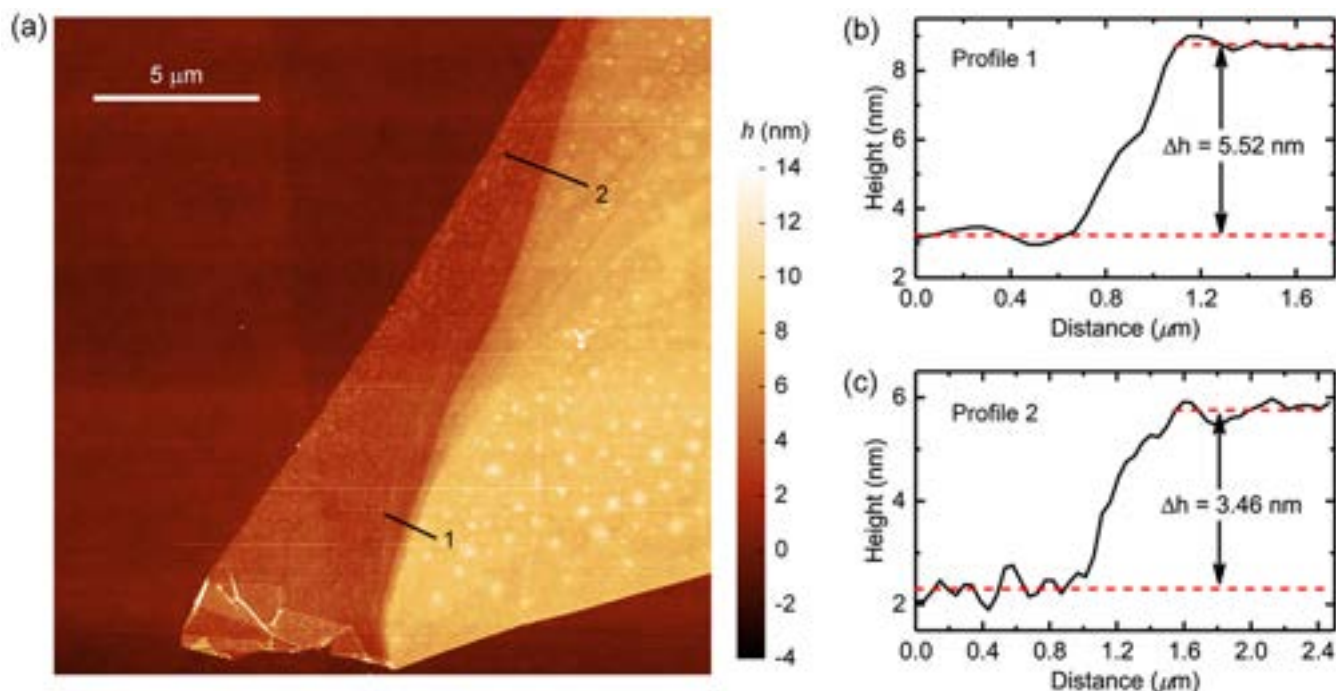
Figure 2. (a) AFM image of 1L−ML-WSe$_2$ LMJ. (b, c) Height profiles along (b) line 1 and (c) line 2 taken across the LMJ.

the layer breathing modes (LBM) are parallel to the normal.[98−102]

The position of the highest frequency C peak, Pos(C$_{N,1}$), can be used to derive N as:[15,99]

$$N = \frac{\pi}{2 \cos^{-1}[\text{Pos}(C_{N,1})/\text{Pos}(C)_\infty]} \tag{1}$$

where Pos(C)$_\infty$ corresponds to B-WSe$_2$. Figure 1b gives Pos(C)$_\infty$ ∼ 24.4 ± 0.06 cm^{-1}. The orange spectrum in Figure 1b has Pos(C$_{N,1}$) ∼ 24.0 ± 0.06 cm^{-1}. From eq 1 we get N ∼ 10 ± 1. The red spectrum in Figure 1b has Pos(C$_{N,1}$) ∼ 23.8 ± 0.06 cm^{-1}; thus, N∼ 7. Figure 1b for N = 7 also shows one LBM at Pos(LBM$_{7,1}$) ∼ 9.1 ± 0.06 cm^{-1} and an additional Pos(C$_{7,2}$) ∼ 19.1 ± 0.06 cm^{-1}, while for 10L-WSe$_2$ we have Pos(LBM$_{10,1}$) ∼ 7.5 ± 0.06 cm^{-1} and Pos(C$_{10,2}$) ∼ 21.2 ± 0.06 cm^{-1}. In Methods we report a detailed discussion of the spectral fitting accuracy and its influence on N.

Figure 1c plots the high-frequency (200−300 cm^{-1}) Raman spectra. For 1L-WSe$_2$, a single peak is observed ∼250 cm^{-1}, associated with the two degenerate, first-order A and E Raman modes.[28,103−107] In B-WSe$_2$, the spectra show a split for the E$^1_{2g}$ and A$_{1g}$ modes due to a red (blue) shift in the E$^1_{2g}$ (A$_{1g}$) mode with increasing N.[104−106] The broad peak ∼260 cm^{-1} can be deconvolved into 2LA(M) and A(M) bands.[105,107] The 2LA(M) mode ∼262 cm^{-1} corresponds to the overtone of the LA phonon branch at the M point of the Brillouin zone (BZ),[105,107] whereas the A(M) mode ∼258 cm^{-1} corresponds to the A-symmetry optical branch at the M point of the BZ.[105,107] The E(M) mode ∼242 cm^{-1} creates an asymmetry in the lower energy shoulder of E$^1_{2g}$+A$_{1g}$.[105,107] This mode red shifts with increasing N.[104−106]

Figure 2a is an AFM image of the 1L−ML-WSe$_2$ LMJ. The line profiles taken in two different parts of the LMJ (Figures.2b,c) show that the ML regions are predominantly N ∼ 10 (profile 1) and N ∼ 7 (profile 2), consistent with the Raman estimate, separated from the ∼1L region by a sub-μm-

wide N ∼ 6 strip. For the estimation of N, we consider a 1L-WSe$_2$ thickness ∼0.6 nm.[31] As the peak positions of the indirect band gap transitions in the photoluminescence (PL) spectrum of ML-WSe$_2$ remain unchanged within ∼1 meV for $N \gtrsim 5$,[8,84] we do not differentiate the 6,7,10L regions in our subsequent analysis, and we refer to these collectively as 6−10L.

Our TR-PEEM setup employs 2.41 eV (515 nm) pump and 3.61 eV (343 nm) probe pulses, with an instrumental response function (IRF) Full Width at Half-Maximum (FWHM) ∼55 fs. The fluences of the pump and probe pulses are 14 and 1 μJ cm^{-2}, respectively. Fluence-dependent measurements indicate that pump and probe interactions with the sample involve one and two photons, respectively (Supporting Information). According to the band structures of 1L- and B-WSe$_2$ (Figure 3),[108] the
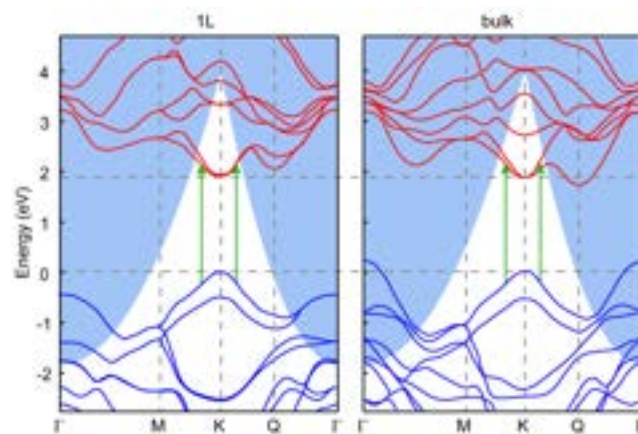

Figure 3. Band structures of 1L- and B-WSe$_2$ from ref 108. B-WSe$_2$ serves as a model for the 6−10L-WSe$_2$ regions. The 1L−7L WSe$_2$ LMJ has type-I band alignment, with CBM and VBM residing on 7L-WSe$_2$. The blue regions are the two-photon probe windows, as required by in-plane momentum conservation within which photoemission occurs.
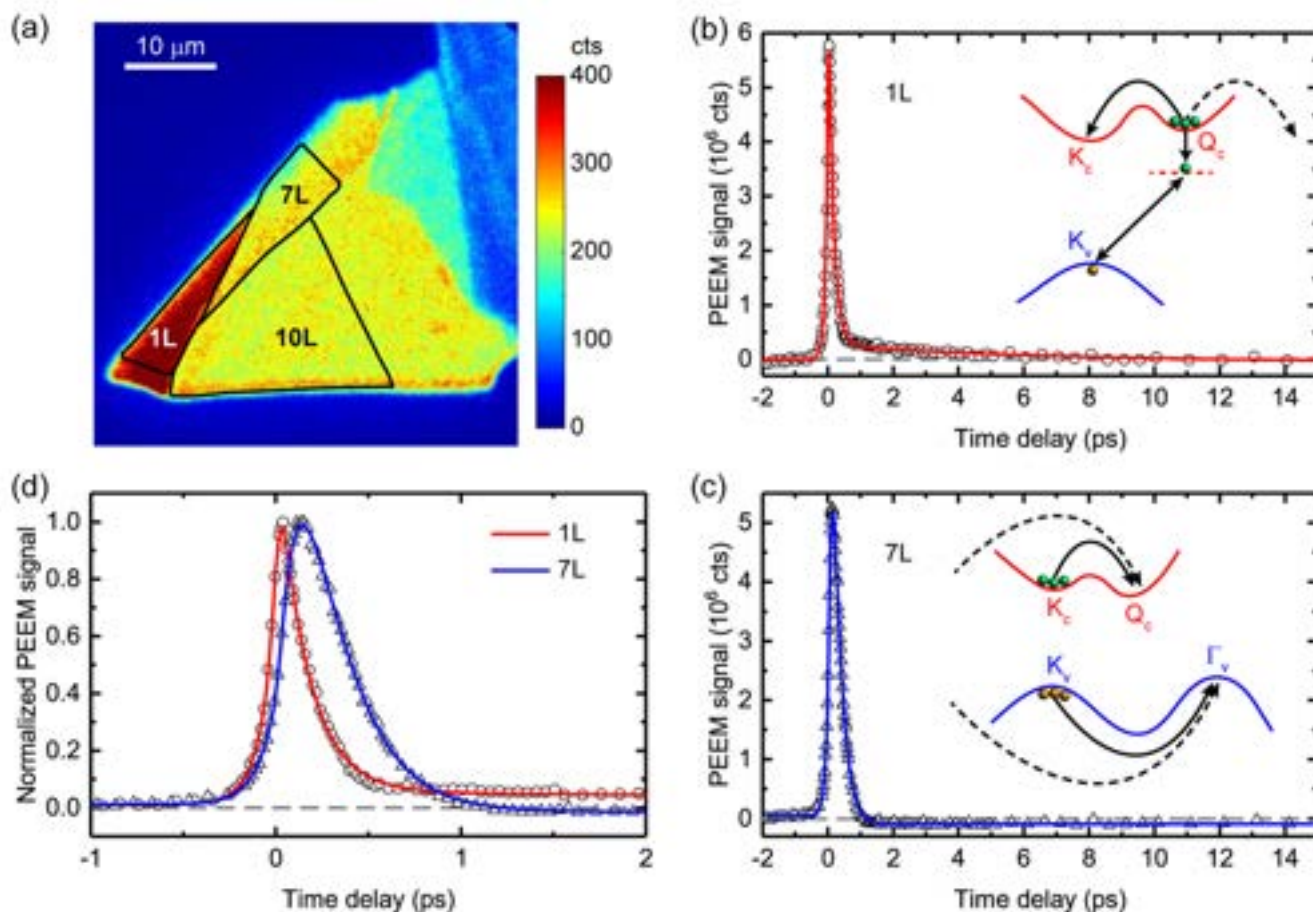
Figure 4. (a) PEEM image of 1L-ML-WSe$_2$ at 0 fs time delay. (b) Spatially integrated time-dependent PEEM signal from 1L-WSe$_2$. The inset shows e cooling, dark exciton formation, and subsequent exciton−exciton annihilation within 1L-WSe$_2$, which leads to the biexponential decay. Interfacial e transfer to ML-WSe$_2$ (dashed line) is energetically possible but not observed. (c) Spatially integrated time-dependent PEEM signal from 7L-WSe$_2$. The inset shows pathways for e and h cooling within 7L-WSe$_2$, as well as interfacial charge transfer from 1L-WSe$_2$ (dashed lines). The exponential rise and decay of the PEEM signal are assigned to e cooling and interfacial h transfer, respectively. (d) Magnified view of normalized time traces of 1L- and 7L-WSe$_2$ regions at short (<2 ps) time delays. At negative time delays the UV probe arrives at the sample before the pump. The gray dashed lines in (b−d) mark the zero baseline.

latter being a model for 6−10L-WSe$_2$, photoexcitation at 2.41 eV is a one-photon process at the K valley. Due to the need to conserve lateral momentum in photoemission, the K valleys of 1L- and B-WSe$_2$ lie beyond the two-photon UV probe window. The probe windows in Figure 3 are calculated based on ionization potentials of 5.38 and 4.98 eV for 1L- and B-WSe$_2$, respectively.[109] Therefore, the dynamics of the K valley do not contribute to the PEEM signal. Instead, this originates from Q valleys,[94] which reside within the probe window. Following the above band gap photoexcitation of 1L-WSe$_2$ near the K valley, e scatters to the Q valley by carrier thermalization. This process, previously shown to occur on a ∼10 fs time scale in TMDs,[110] takes place within our IRF FWHM and leads to the initial population of the conduction band Q valley. The buildup of e population in the Q valley ceases after carrier thermalization is completed on the ∼10 fs time scale.[110] As a result of the well-defined probe window (Figure 3) and the restricted regions in the first BZ to which carriers can flow following photoexcitation, energy and/or momentum filtering are not required and not critical for the interpretation of the observed dynamics. The use of two-photon UV probing[94,111] yields dynamics in regions of k space otherwise inaccessible via a one-photon probe.[112]

The interaction with the UV probe at 3.61 eV must be a two-photon process, since one-photon probing does not access the region of the conduction band within which the photoexcited e resides (see Supporting Information). The Q valley lies within the probe window and can be populated within the width of the IRF by intervalley scattering on a ∼10 fs time scale,[110] as explained in Supporting Information. For 7L-WSe$_2$, the VBM at the Γ point also lies within the probe window and can therefore contribute to the PEEM signal.

The sub-80 nm spatial resolution of our TR-PEEM[94,95] is well-suited for resolving the carrier dynamics of 1−7L-WSe$_2$ LMJ. The TR-PEEM image acquired at 0 fs time delay (Figure 4a) shows that the signal for 1L-WSe$_2$ is ∼50% larger than that for 7L-WSe$_2$. This is consistent with the previously reported nonmonotonic change in the PEEM intensity as a function of N attributed to abrupt changes in the UV photoionization cross-section with N.[113] To investigate the ultrafast dynamics of the LMJ, we measure spatially integrated time-dependent PEEM from 1L-WSe$_2$ (Figure 4b) and 7L-WSe$_2$ (Figure 4c), with pump and probe fluences of 14 and 1 μJ cm^{-2}, respectively.

TR-PEEM of 1L-WSe$_2$ exhibits a biexponential decay, with time constants $\tau_1^{1L} = 0.16 \pm 0.01$ ps and $\tau_2^{1L} = 5.13 \pm 0.97$ ps, and an amplitude ratio $A_1^{1L}/A_2^{1L} = 24.9 \pm 2.4$. For 7L-WSe$_2$, TR-

PEEM shows a delayed rise followed by a decay, with $\tau_r^{7L} = 0.11 \pm 0.01$ ps and $\tau_d^{7L} = 0.22 \pm 0.01$ ps, respectively (Figure 4d). The decay is followed by a weak, long-lived negative offset due to the generation of excess h in 7L-WSe$_2$. The peak of the 1L-WSe$_2$ signal (Figure 4d) is delayed ~31 fs relative to time-zero. However, this does not reflect the finite time for intervalley e scattering from K to Q valley, estimated to occur with a time constant of 16 ± 5 fs.[114] Instead, it arises from finite IRF FHWM ~ 54 fs, obtained from the global fit. This is consistent with ref 115, which showed that K and Q valleys are simultaneously populated by above-band-gap, 2.48 eV photoexcitation.[115] Our ~50 fs time resolution does not allow the time scale for K to Q intervalley scattering to be precisely determined, since it occurs within it. On the other hand, the delay in the peak of the 7L-WSe$_2$ signal can be ascribed to the ~0.1 ps K to Q intervalley e scattering (see below).

Following our previous TR-PEEM investigation of CVD-grown 1L-WSe$_2$,[94] we assign τ_1^{1L} to depopulation of the Q valley, based on intervalley scattering to the K valley being energetically favorable (Figure 3), and τ_2^{1L} to exciton−exciton annihilation, based on the observed acceleration of the annihilation process with higher excitation density.[116,117] The PEEM signal does not decay completely on the sub-ps time scale. At a 500 fs delay, it is still ~10% of the peak signal. Hence, after initial e cooling on the time scale of τ_1^{1L}, there exists a small, but non-negligible, residual population in the Q valley, suggestive of dark exciton formation.[115,118] The observed dynamics differ from those of previous works that employed resonant excitation of the A exciton transition,[114,115] reporting a ps time scale.[114,115] Our experiments employ above-band-gap excitation at 2.41 eV, where free carriers dominate the initial ultrafast dynamics.

We now consider the various possible pathways by which e can leave the conduction band Q valley of 1L-WSe$_2$. Control experiments performed on an isolated 1L-WSe$_2$ (see below) are then used to eliminate some of these pathways. First, since the K valley is lower than the Q valley in the CB of 1L-WSe$_2$,[108,119,120] carrier cooling via intervalley scattering[28] leads to the transfer of e population from the Q to the K valley. Second, Q valley e can transfer across the LMJ interface to the lower-lying Q valley of 7L-WSe$_2$. Third, they can form dark excitons,[115,118] comprising Q valley e and K valley h (VBM), where e and h have different momenta, therefore cannot undergo radiative recombination. The observed ~0.3 ps delay, assigned to indirect exciton formation following above-band-gap excitation of 1L-WSe$_2$,[115] is consistent with our τ_1^{1L}. These dark excitons, which reside in the probe window and have nonvanishing momenta, can subsequently undergo exciton−exciton annihilation,[118] thereby resulting in the observed few-ps decay. A similar Auger-mediated annihilation dynamics of dark excitons in 1L-WSe$_2$ was identified by time-resolved mid-infrared (~6−9 μm) probing of intraexcitonic transitions.[118] Global fitting of the time traces at different excitation fluences (11−21 μJ cm^{-2}) yields the annihilation rate constant γ = 0.46 ± 0.02 cm^2 s^{-1} (see Supporting Information for details), consistent with γ ~ 0.35 cm^2 s^{-1} obtained from a combination of PL spectroscopy and Monte Carlo simulations of 1L-WSe$_2$,[121] and with those obtained from time-resolved optical microscopy for 1L-MoSe$_2$ (0.33 ± 0.06 cm^2 s^{-1})[122] and 1L-WS$_2$ (0.41 ± 0.02 cm^2 s^{-1}).[116]

To understand the temporal behavior of the TR-PEEM signal for 7L-WSe$_2$ (Figure 4c), we first note that the CBM and VBM of ML-WSe$_2$, located at the Q and Γ valleys, respectively, both reside within the probe window (Figure 3). The Q valley is located 150 meV below the K valley in the CB, while the Γ valley

lies 180 meV above the K valley in the VB.[108] Photoexcitation of 7L-WSe$_2$ at 2.41 eV occurs in the vicinity of the K valley and is followed by carrier cooling, channeling e from K to Q (CBM), and h from K to Γ (VBM). Since the acquisition of TR-PEEM images involves referencing to the PEEM image collected with long (250 ps) temporal separation of the pump and probe pulses (see Methods), the appearance of e (h) in the probe window leads to a rise (decay) of the TR-PEEM signal. The 7L-WSe$_2$ signal also indicates charge transfer across the 1L−7L-WSe$_2$ interface. Since CBM and VBM of 7L-WSe$_2$ both reside in the probe window, e (h) transfer would result in the appearance of excess e (h) in 7L-WSe$_2$, in turn giving rise to a positive (negative) offset in the TR-PEEM signal. Figure 4c shows a negative baseline offset at time delays >1 ps, suggesting the presence of sub-ps h transfer across the LMJ. According to scanning tunneling spectroscopy, the VB offset between 1L- and 2L-WSe$_2$ is 0.12 eV,[80] thus making h transfer from 1L- to ML-WSe$_2$ energetically favorable. As such, we assign the $\tau_d^{7L} \sim 0.22$ ps component to the h transfer. On the other hand, we attribute $\tau_r^{7L} \sim 0.11$ ps to e cooling via K → Q intervalley scattering, slower than 1L-WSe$_2$. Ref 123 analyzed the temperature-dependent optical reflectance of 1L- and 2L-WS$_2$ to extract their homogeneous line widths. Their results suggest enhanced exciton−phonon scattering in 2L-WS$_2$ compared to 1L-WS$_2$. However, homogeneous line widths give optical dephasing times,[124] and do not directly probe intervalley scattering time scales.[125] A more direct comparison of K to Q intervalley scattering times can be obtained from time- and angle-resolved photoemission spectroscopy measurements of 1L-WSe$_2$[115] and B-WSe$_2$.[126] While photoexcitation of 1L-WSe$_2$ does not reveal any noticeable delay between the population of the K and Q valleys,[115] photoexcitation of B-WSe$_2$ yields a delayed appearance of the Q valley, with its population peaking ~0.2 ps after photoexcitation, from which an intervalley scattering time scale ~70 ± 15 fs was inferred.[126] These results are consistent with ours, which suggest a more rapid K to Q intervalley scattering for 1L-WSe$_2$ than for 7L-WSe$_2$. The few-ps decay observed in 1L-WSe$_2$, assigned to exciton−exciton annihilation,[94] is absent because the small exciton binding energies of B-TMDs, typically on the order of 10 meV,[126−128] do not support stable excitons in 7L-WSe$_2$ at room temperature.

The negative offset in Figure 4c,d, assigned to h transfer, could also be due to matrix element effects,[129] causing the photo-ionization cross-section to be larger for the CB Q valley than the VB Γ valley. To verify the occurrence of ultrafast h transfer and to elucidate possible ultrafast e or exciton transfer across the 1L−7L WSe$_2$ interface, we perform TR-PEEM on an isolated 1L-WSe$_2$ flake under identical experimental conditions (see Supporting Information). This cannot exhibit any charge or energy transfer dynamics. Its TR-PEEM time trace, shown in the Supporting Information, can be fit to a biexponential decay, with a fast $\tau_1^{1L} = 0.13 \pm 0.01$ ps, a slow $\tau_2^{1L} = 3.28 \pm 0.10$ ps, and $A_1^{1L}/A_2^{1L} = 9.0 \pm 0.4$. As for the 1L-WSe$_2$ in our LMJ, the fast and slow decays are attributed to e leaving the Q valley and exciton−exciton annihilation, respectively. Global fitting of the slow decay component at different excitation fluences yields γ ~ 0.30 ± 0.04 cm^2 s^{-1} (see Supporting Information). The nearly identical τ_1^{1L} for both isolated 1L-WSe$_2$ and that in the LMJ rules out e transfer as an additional deactivation pathway for the Q valley e of 1L-WSe$_2$ in our LMJ. Compared with isolated 1L-WSe$_2$, the slower exciton population decay τ_2^{1L} of the 1L-WSe$_2$ in our LMJ excludes the possibility of ultrafast exciton transfer occurring at the 1L−7L-WSe$_2$ LMJ, which would accelerate the
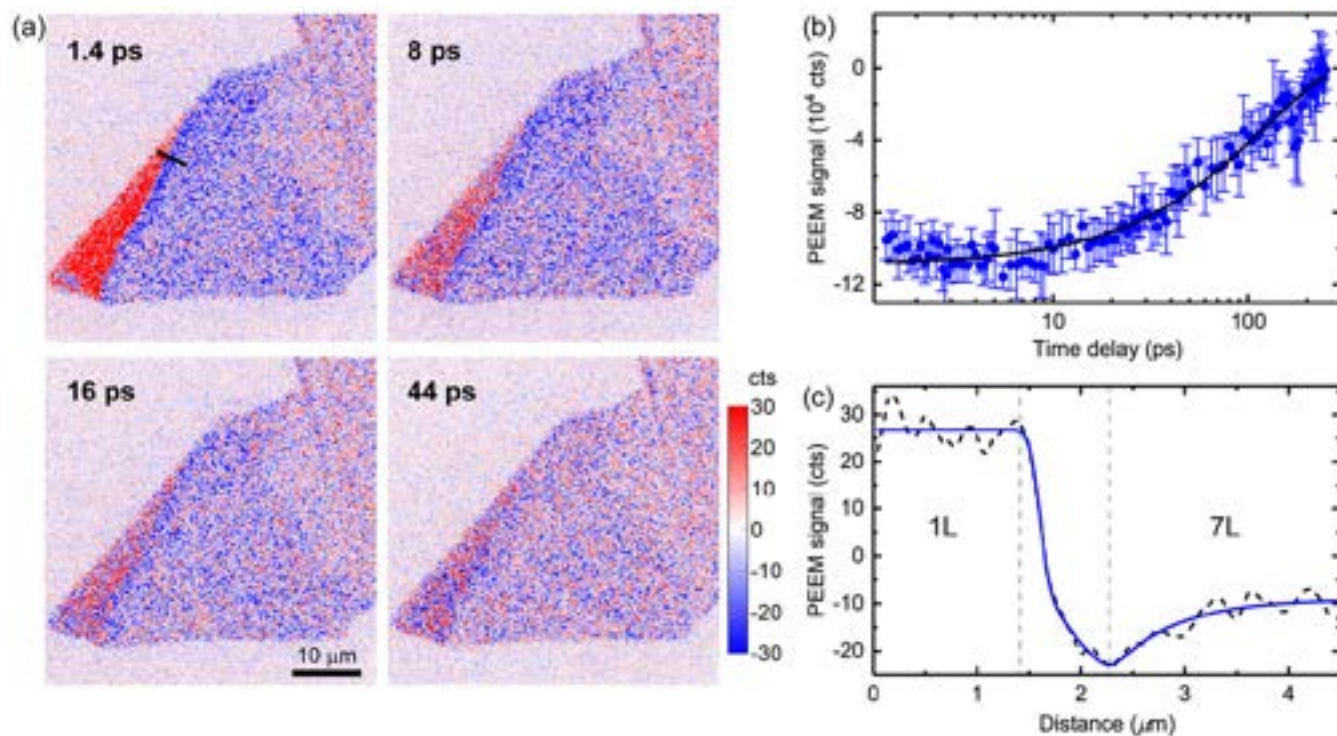
Figure 5. (a) Differential PEEM images with time delays from 1.4 to 44 ps. (b) Time trace of 7L-WSe$_2$ PEEM with a pump−probe time delay up to 250 ps, undergoing an exponential decay. The black line shows the fit to a single-exponential decay. (c) PEEM signal profile along the black line on the 1.4 ps image in (a). The PEEM signal changes from positive in the 1L region to negative in 7L, and has a rise within the 7L region, fitted with an exponential function.

decay of the exciton component of the TR-PEEM signal. Instead, the slower exciton population decay of 1L-WSe$_2$ in our LMJ is consistent with ultrafast h transfer depleting the initial density of dark excitons, hence decelerating exciton−exciton annihilation.[116] A lower initial exciton density also reduces the relative contribution of exciton−exciton annihilation to the overall PEEM signal, thereby accounting for the larger A_1^{1L}/A_2^{1L} for 1L-WSe$_2$ in our LMJ. Comparing A_1^{1L}/A_2^{1L} for LMJ and the isolated flake, we find that the initial exciton density in the LMJ is ∼40% that of the isolated flake. A similar reduction in the initial exciton density is obtained when one considers the measured τ_2^{1L} and γ for both samples (see Supporting Information). Our interpretation that the observed negative offset in the 7L region of 1L−7L-WSe$_2$ arises from interfacial h transfer is consistent with a previous time-resolved photoemission study of bulk-WSe$_2$,[126] which did not observe the 0.22 ps decay component that we ascribe to h transfer. Instead, the dynamics reported in ref 126 are dominated by a long-lived (tens of ps) population of Q valley e. Our control experiment on an isolated 1L-WSe$_2$ flake (see the Supporting Information) proves that e transfer across the 1L−7L-WSe$_2$ interface does not occur, thus allowing us to attribute any differences in the ps dynamics of excitons to h transfer, giving rise to a lower initial exciton density.

The absence of exciton transfer across the interface, despite the type-I band alignment of our 1L−7L-WSe$_2$ LMJ, can be rationalized in terms of the large exciton binding energy (0.37 eV)[130] of 1L-WSe$_2$, the vanishingly small exciton binding energy of 7L-WSe$_2$,[127] and the small VB and CB offsets at the 1L−7L-WSe$_2$ LMJ. These factors make exciton transfer energetically unfavorable. The apparent absence of interfacial e transfer requires further investigation. We note that exciton formation does not explain the absence of e transfer across the LMJ, since h

transfer may also be similarly impeded. One possible explanation is that ultrafast K to Q intervalley e scattering within 7L-WSe$_2$, with $\tau_r^{7L} = 0.11 \pm 0.01$ ps, could inhibit e transfer by Pauli blocking. Given that e transfer is mediated by the strong interlayer coupling at the Q valley,[69] it is conceivable that the population of the Q valley of 7L-WSe$_2$ could inhibit e transfer across the LMJ.

The negative baseline offset that appears in the TR-PEEM time trace of 7L-WSe$_2$ in our LMJ (Figure 4c) points to the existence of a long-lived h population on 7L-WSe$_2$. Figure 5a shows the TR-PEEM images for pump−probe time delays >1 ps. Extending the pump−probe time delay to 250 ps shows that the negative offset decays with a time constant ∼108 ± 9 ps (Figure 5b), signaling the h disappearance from 7L-WSe$_2$ on this time scale. TR-PEEM is unable to detect carrier recombination within 7L-WSe$_2$ because both its VBM and CBM are within the probe window.

The disappearance of h from the probe window is thus attributed to carrier recombination across the 1L−7L junction. To the best of our knowledge, the interfacial carrier recombination times for TMD 1L−ML LMJs and lateral TMD LMHs were not previously reported. The ∼100 ps recombination time is in the range observed for vertical TMD LMHs.[61,64,131] Inspection of the TR-PEEM images collected for the 7L-WSe$_2$ region at >1 ps time delays, when carrier cooling no longer contributes to the signal, reveals h accumulation at the 1L−7L-WSe$_2$ interface (Figure 5a). The higher h density at the interface can also be seen from the lineout of the TR-PEEM signal (Figure 5c), which reveals a decrease in h density with distance from the 1L−7L-WSe$_2$ interface. This might be assigned to the depletion region that exists at the 1L−7L-WSe$_2$ interface. Fitting the h density distance dependence (see
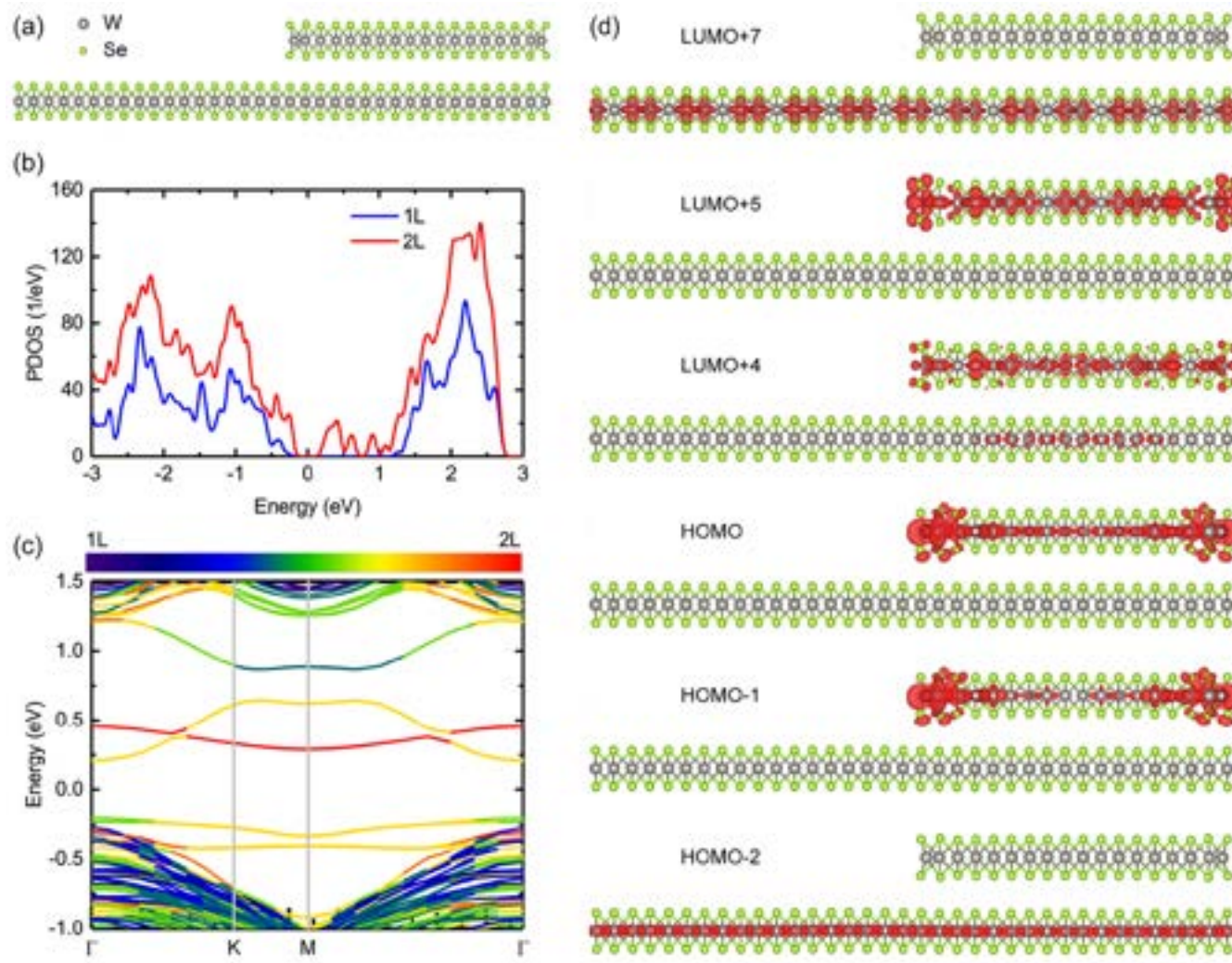
Figure 6. (a) Side view of optimized geometry of 1L−2L-WSe$_2$ LMJ. (b) Partial density of states and (c) band structure of 1L−2L-WSe$_2$. The states in the band gap represent edge states. The zero energy corresponds to E_F. The band structure is color coded to show the relative contributions of the 1L and 2L regions to the individual bands. (d) Charge densities of the various states involved in the ultrafast dynamics at the 1L−2L-WSe$_2$ LMJ. The isosurface is set at 0.001 e/Å^3.

Supporting Information) suggests a depletion width ∼0.60 ± 0.17 μm, similar to the 0.32 μm for 1L-WSe$_2$−1L-MoS$_2$ LMJ.[132] The existence of a depletion region is consistent with h transfer across the LMJ, since it would not exist without excess carriers.[132]

To get further insights into the ultrafast dynamics of our LMJ, we perform *ab initio* quantum dynamics on a model 1L−2L-WSe$_2$ LMJ (Figure 6a; see Supporting Information for details). The 162-atom structure was previously used to study electronic properties of WSe$_2$ LMJs, exhibiting properties similar to those of structures with a larger *N*.[75] Including all 7 layers would make the calculations prohibitively expensive computationally. The bottom 1L-WSe$_2$ contains 108 atoms periodically replicated in two dimensions. To create a 2L-WSe$_2$, a second layer is added on half of the bottom 1L-WSe$_2$. Geometry optimization gives a Se⋯Se distance ∼3.36 Å between the two 1L-WSe$_2$, in agreement with ref 75. The calculated density of e states and band structure for the model 1L−2L-WSe$_2$ LMJ are shown in Figure 6b,c, respectively. The charge densities of the key states involved in the excitation dynamics are listed in Figure 6d. The simulated system can be viewed either as a 108-atom bottom 1L-WSe$_2$

with a 54-atom top half-layer or as a 54-atom 1L-WSe$_2$ on the left and a 108-atom 2L-WSe$_2$ on the right. Necessarily, the top half-layer contains edges, which create defect states inside the band gap of 1L−2L-WSe$_2$. The defect states appear midgap (Figure 6b) and can be identified by the flat band dispersion (Figure 6c) as well as by their charge densities (see the Supporting Information). Because the size of the top layer is large in experiments, on the order of ∼1 μm (Figure 1a), the relative contribution of edges to the overall dynamics is likely insignificant. Therefore, the defect states created by edges are excluded from the simulations.

We simulate h and e dynamics to provide insights into why only interfacial h transfer is observed, without interfacial e transfer, even though both processes are energetically favorable. The simulated h and e dynamics are shown in Figure 7a,b, respectively. h transfer occurs from the top of the 1L-WSe$_2$ VB, represented by the HOMO-2 orbital, to the top of the 2L-WSe$_2$ VB region, represented by the HOMO (Figure 6d). The simulations give a time constant ∼339 fs for h transfer, in agreement with the measured τ_d^{7L} ∼ 0.22 ps. The transfer is ultrafast because it occurs through a dense manifold of VB states
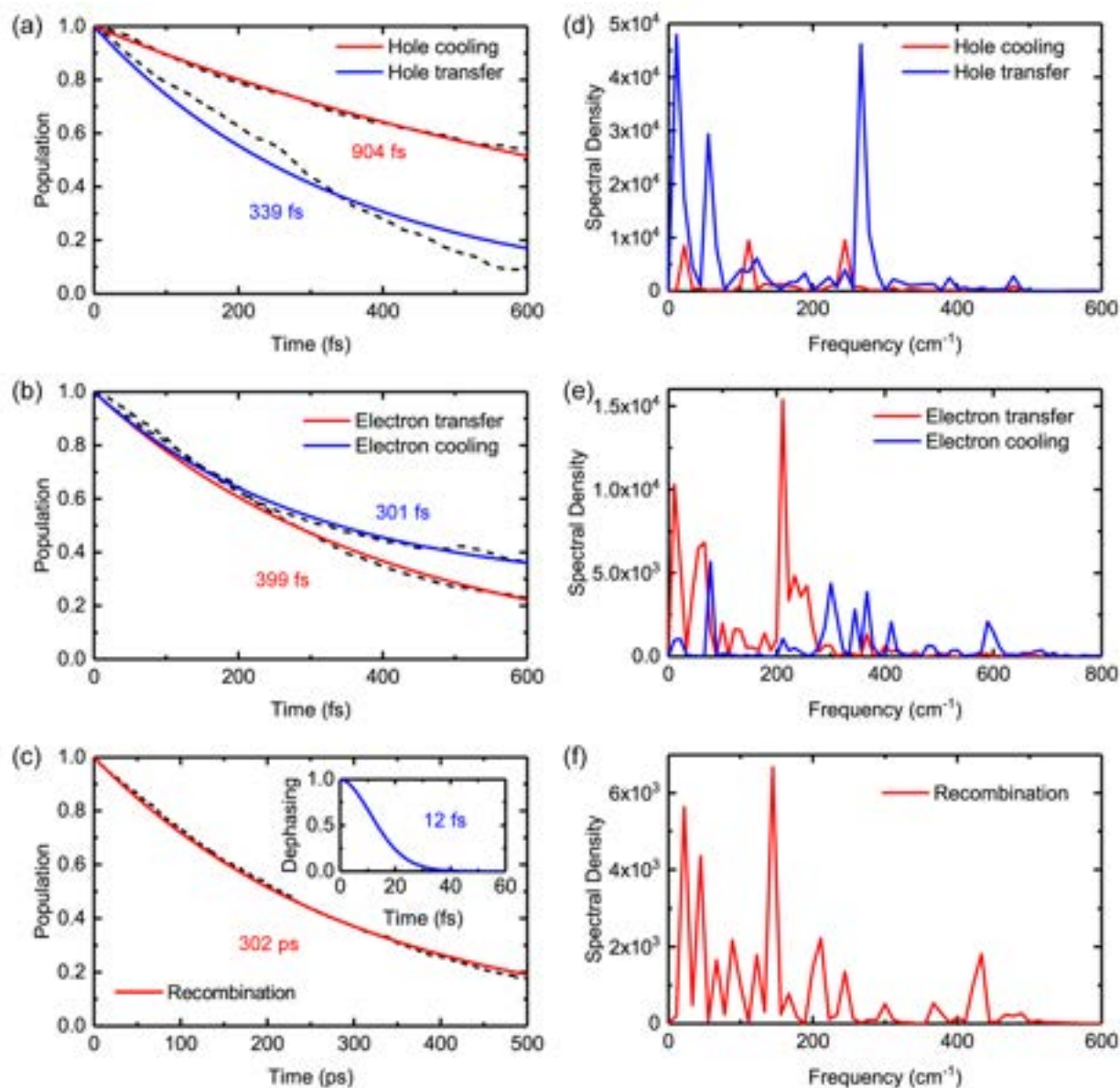
Figure 7. Simulated dynamics for (a) h transfer and cooling, (b) e transfer and cooling, and (c) interfacial e−h recombination. Spectral densities characterizing phonon modes involved in the charge dynamics for (d) h transfer and cooling, (e) e transfer and cooling, and (f) e−h recombination.

(Figure 6c). The average absolute nonadiabatic coupling between HOMO-2 and HOMO is 10.5 meV. The simulated time constant for h cooling within 2L-WSe$_2$ is 904 fs, ∼3× longer than the interfacial h transfer time. Hence, h cooling might not be observed experimentally because it is outpaced by interfacial h transfer.

Beyond h transfer, the simulations also elucidate why interfacial e transfer is not observed despite the type-I band alignment at the 1L−7L-WSe$_2$ interface. The simulated time constant for e transfer from the CBM of 1L-WSe$_2$ (LUMO+7 in Figure 6d) to the CBM of 2L-WSe$_2$ (LUMO+4) is 399 fs (Figure 7b), whereas that for e cooling within 2L-WSe$_2$ is 301 fs, i.e., ∼1.3× faster than e transfer. Thus, e transfer is suppressed at the expense of e cooling. Given that e transfer is mediated by the strong interlayer coupling at the Q valley,[69] it is conceivable that the population of the Q valley of 7L-WSe$_2$ by e cooling could inhibit e transfer across the LMJ.

To explain charge recombination being 2 orders of magnitude slower compared to interfacial h transfer, we model recombination across the 1L−7L-WSe$_2$ interface by considering the LUMO+7 and HOMO orbitals (Figure 6d), which correspond to the CBM of 1L-WSe$_2$ and the VBM of 2L-WSe$_2$, respectively. The simulations give a recombination time ∼302 ps (Figure 7c), consistent with the experimental ∼108 ps. Charge recombination is slower than transfer, for several reasons. First, recombination occurs across a large energy gap (1.31 eV). Second, the nonadiabatic coupling between the orbitals that participate in charge recombination (1.35 meV) is 1 order of magnitude smaller than that between the orbitals that participate in e (12.2 meV) and h (10.5 meV) transfer. Third, recombination involves a rapid 12 fs loss of quantum coherence (Figure 7c, inset), which slows down quantum dynamics. This is exemplified by the quantum Zeno effect,[133] whereby transitions stop completely if one attempts to measure continuously and

precisely the quantum state of the system, giving rise to infinitely fast coherence loss.[133]

The simulations also provide insights into the relative importance of carrier cooling vs transfer for e and h. The frequencies of the phonon modes that accommodate the excess energy lost by the electronic subsystem during these non-radiative processes are given in Figure 7d,e for h and e transfer, respectively, and in Figure 7f for e−h recombination. These spectral densities are obtained as Fourier transforms of the phonon-induced fluctuations in the corresponding energy gaps. A higher intensity of a peak at a given frequency and the presence of multiple phonon modes favor stronger nonadiabatic coupling. Figure 7d shows that the intensity of major phonon modes for h transfer is ∼5× larger than that for h cooling, leading to stronger nonadiabatic coupling, thus faster h transfer. The situation changes for e dynamics. Even though the peaks are higher for e transfer than for cooling, the difference is less pronounced. In addition, e cooling is promoted by several high-frequency modes ∼300−400 and 600 cm^{-1}, which do not participate in e transfer. As a result, e cooling is faster than transfer (Figure 7b). The peak ∼267 cm^{-1}, contributing strongly to the h transfer process, can be assigned to the 2LA(M) mode, observed at ∼260 cm^{-1} in the Raman spectra (Figure 1c). The frequencies <250 cm^{-1} can be attributed to various transverse and longitudinal acoustic modes, shear modes, and their overtones or combinations. Long-wavelength acoustic modes influence charge wave functions over nm scales, facilitating charge transfer.[68,95] Multiple vibrations contribute to the charge dynamics because the interface between 1L and ML regions breaks the symmetry and relaxes electron−phonon coupling selection rules. The e-vibrational coupling matrix elements, $\langle i|\nabla_r|j\rangle$, for nonradiative charge transfer and recombination are different from the Raman matrix elements[134] and have weaker selection rules, because optical spectra are determined by operators with high symmetries describing, e.g., linearly polarized light, while the gradients with respect to vibrational motions, ∇_r, represent many different symmetries. This fact rationalizes why more modes participate in the charge dynamics than in the Raman spectra.

The salient experimental and theoretical observations are summarized below.

(1) The sub-ps decay constants for the 1L-WSe$_2$ region of the 1L−7L-WSe$_2$ LMJ (τ_1^{1L} = 0.16 ± 0.01 ps) and for an isolated 1L-WSe$_2$ flake (τ_1^{1L} = 0.13 ± 0.01 ps) are similar. τ_1^{1L} is assigned to the depopulation of the Q valley in 1L-WSe$_2$. The similarity of τ_1^{1L} rules out sub-ps e transfer from the 1L- to the 7L-WSe$_2$ region of the LMJ, which would accelerate the decay.

(2) The few-ps decay of 1L-WSe$_2$ is slower for the 1L−7L-WSe$_2$ LMJ (τ_2^{1L} = 5.13 ± 0.97 ps) than for the isolated 1L-WSe$_2$ flake (τ_2^{1L} = 3.28 ± 0.10 ps). τ_2^{1L} is assigned to exciton−exciton annihilation in 1L-WSe$_2$. The slower exciton−exciton annihilation for the LMJ than the isolated flake, according to second-order kinetics,[116,117] is suggestive of the initial exciton density being lower in the LMJ than in the isolated flake. Since e do not transfer from 1L- to 7L-WSe$_2$ in the LMJ, its lower initial exciton density suggests h transfer from 1L- to 7L-WSe$_2$.

(3) The 7L-WSe$_2$ region of the LMJ exhibits an ultrafast decay (τ_d^{7L} = 0.22 ± 0.01 ps) and a long-lived, >100 ps, negative offset. This implies h transfer, because both CBM and VBM of 7L-WSe$_2$ reside in the probe window, such that

the appearance of excess h in 7L-WSe$_2$ would yield a lower PEEM signal, resulting in a negative offset, that could also arise from matrix element effects.[129]

(4) Ab initio nonadiabatic molecular dynamics simulations on a 1L−2L-WSe$_2$ LMJ (used as a model for the experimental 1L−7L-WSe$_2$ LMJ) reveal that h transfer from 1L- to 2L-WSe$_2$ is ∼3× faster than h cooling within 2L-WSe$_2$. Hence, we assign the ultrafast decay in the 7L-WSe$_2$ region to h transfer from 1L-WSe$_2$ instead of h cooling within 7L-WSe$_2$.

(5) A section of the PEEM image normal to the 1L−7L-WSe$_2$ junction reveals a depletion region (Figure 5a). This, and the negative PEEM signal, imply h accumulation in 7L-WSe$_2$. A depletion region, by definition, requires the presence of excess carriers.[135]

CONCLUSIONS

We studied the dynamics of photoexcited carriers at the 1L−7L-WSe$_2$ interface using a combination of TR-PEEM and nonadiabatic *ab initio* molecular dynamics. Since the low-energy, 7.22 eV two-photon photoionization probe provides a well-defined probe window and carriers can only flow to restricted regions of the first Brillouin zone, energy and/or momentum resolution are not required for the interpretation of the experimental results. Instead, interpretation of the observed ultrafast dynamics is primarily done by comparing the ultrafast dynamics of the 1l−7L-WSe$_2$ LMJ sample to those of the isolated 1L-WSe$_2$ flake. The experimental and theoretical results suggest interfacial h transfer from 1L- to 7L-WSe$_2$ within the LMJ on an ∼0.2 ps time scale. The resultant excess h density in 7L-WSe$_2$ eventually decays by carrier recombination across the 1L−7L-WSe$_2$ interface on a 100 ps time scale. The experimental time scales for interfacial h transfer and e−h recombination are consistent with *ab initio* quantum dynamics simulations. These results suggest that ML regions alongside 1L ones can influence the ultrafast carrier dynamics of the latter. As such, the analysis of time-resolved data should consider ultrafast charge transfer across the 1L−ML interface as an additional carrier deactivation pathway. Charge transfer does not occur in-plane, unlike lateral LMHs.[70,71] Instead, as the charge density plots in Figure 6d suggest, h transfer involves the shift of h density from the basal plane (HOMO-2), extended over 1L and 2L regions, to the top plane (HOMO), localized on the 2L region. The interfacial charge transfer in 1L−7L-WSe$_2$ is thus more akin to that occurring in vertical LMHs, albeit with chemically identical bottom and top layers. Such a mode of charge transfer is distinctive to LMJs.

The e transfer dynamics of 1L-MoSe$_2$−1L-MoSe$_2$, 1L-WS$_2$−1L-WS$_2$, and 1L-WSe$_2$−1L-WSe$_2$, each with an underlying graphene substrate, was previously reported.[136] However, in ref 136 the underlying graphene substrate also participates in ultrafast charge transfer.[137] While ps interlayer e transfer following above-band gap photoexcitation was resolved in ref 136, the time scale for h transfer to the Γ valley remained elusive. The h dynamics at the Γ valley is of particular interest because the spatial extension of the Γ valley wave functions in the out-of-plane direction makes it to play an important role in mediating interlayer h transfer.[69] Our results yield τ_d^{7L} ∼ 0.2 ps for h transfer to the Γ valley of 7L-WSe$_2$, suggesting that LMJs can also support ultrafast interlayer h transfer.

METHODS

Ultralow-Frequency Raman Spectral Fitting Accuracy. Raman spectroscopy can determine N in TMDs.[98−102] However, accurate estimation for $N > 3$ requires measurements of $\text{Pos}(C_{N,1})$ with high precision (typical shift ranging from 0.05 to 0.3 cm^{-1} vs a typical spectral resolution ~0.6 cm^{-1}). Peak position evaluation with subpixel accuracy can be achieved via spectral fitting. We demonstrate the feasibility of this approach by measuring the changes in $\text{Pos}(C_{N,1})$ in 2−12L-MoS$_2$ (Figure 8). Regions of different thicknesses are identified using optical contrast and confirmed by AFM. $\text{Pos}(C_{N,1})$ is given in
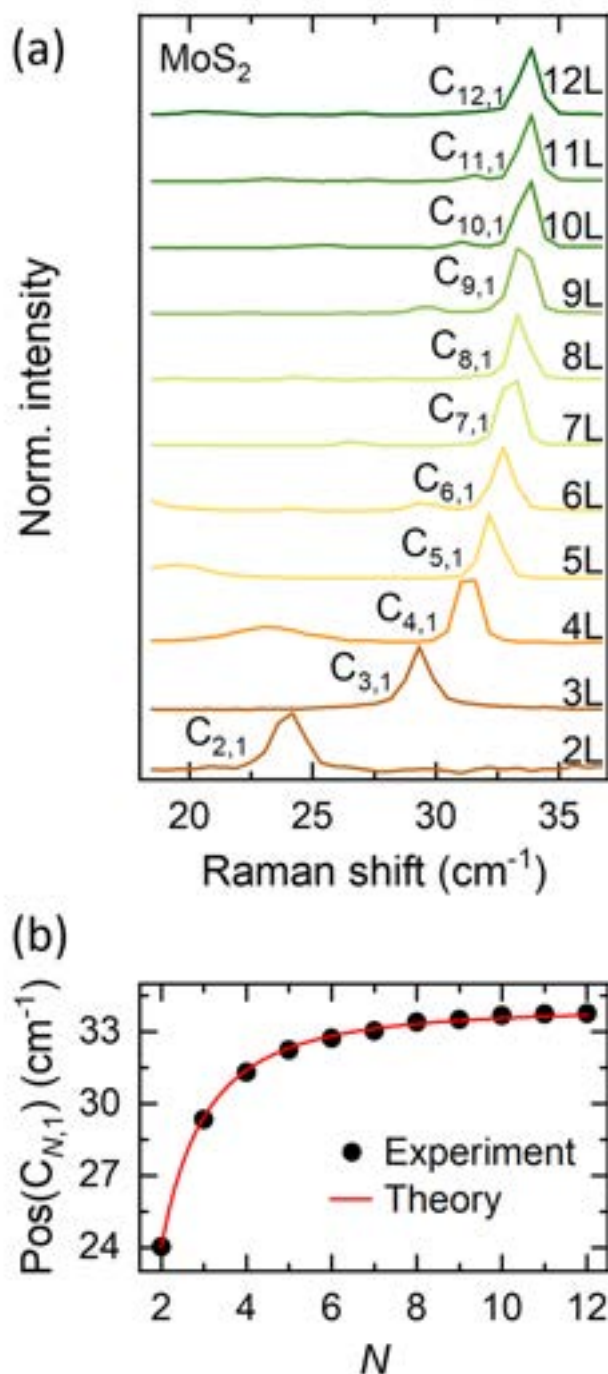
Figure 8b (black circles), showing an increase with N in excellent agreement with eq 1, with $\text{Pos}(C)_\infty \sim 33.99$ cm^{-1}. $C_{11,1}$ and $C_{12,1}$ can be resolved in Figure 8a, even though $\text{Pos}(C_{12,1}) - \text{Pos}(C_{11,1}) \sim 0.02$ cm^{-1}. There are three key factors that contribute an error to $\text{Pos}(C_{N,1})$: (1) general fitting error, (2) statistical error, and (3) subpixel specific fitting error.

First, we evaluate the general fitting error. Figure 9a is an example of spectral fitting, with black circles representing experimental data and
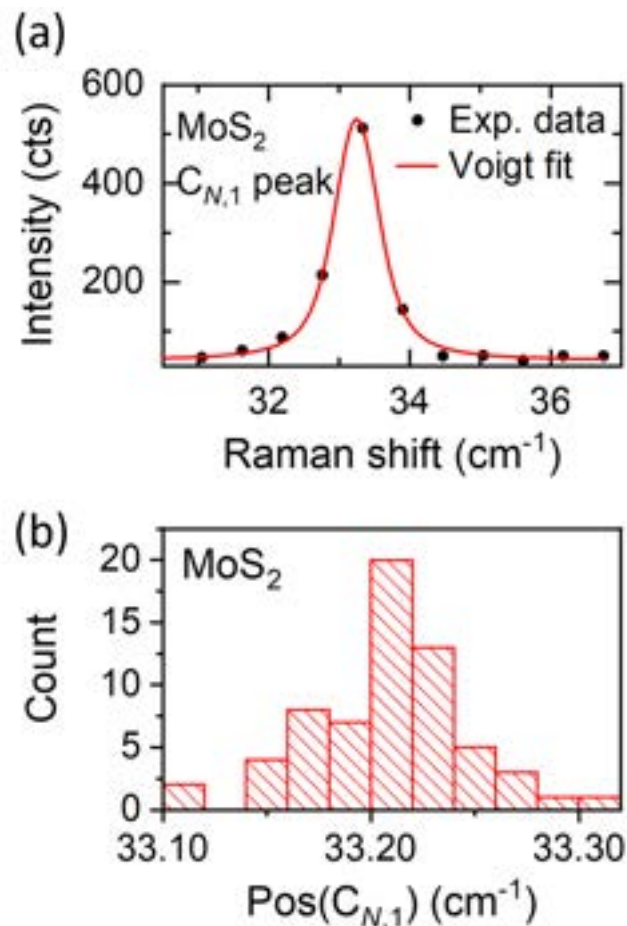

Figure 8. (a) Raman spectra normalized to their maximum intensities showing the $C_{N,1}$ peak in 2−12L-MoS$_2$. (b) $\text{Pos}(C_{N,1})$ vs N: experiments (black circles) are in agreement with eq 1 (red line).

Figure 9. (a) $\text{Pos}(C_{N,1})$ fitting for a $N > 15$ ML-MoS$_2$ flake: black dots, experimental data; red curve, Voigt fit. (b) Histogram showing the variation of $\text{Pos}(C_{N,1})$ by acquiring spectra at 64 different points.

the red line a Voigt fit. The fitted curve is in good agreement with experimental data, with a coefficient of determination $R^2 \sim 0.99$. The typical $\text{Pos}(C_{N,1})$ error is ~0.02 cm^{-1} and likely represents the lower boundary.

Second, we look at statistical error, i.e., variations of $\text{Pos}(C_{N,1})$ in different areas with the same N, which can be caused by changes of material properties (e.g., strain or disorder), as well as random noise on the CCD detector. The latter can have a strong effect on $\text{Pos}(C_{N,1})$ due to the small number of data points (5−7) used for spectral fitting. To evaluate typical values of statistical error, we acquire spectra in 64 areas within a $N > 15$ ML-MoS$_2$. Figure 9b is a histogram of fitted $\text{Pos}(C_{N,1})$, with a mean ~33.2 cm^{-1} and standard deviation ~0.04 cm^{-1}, consistent with other samples.

Third, we consider the error associated with the subpixel fitting. Since $\text{FWHM}(C_{N,1})$ is comparable with the spectral resolution, the extracted $\text{Pos}(C_{N,1})$ can be very sensitive to pixel registry, i.e., microscopic alignment of the light dispersed by grating and CCD pixel array. To investigate this, we record the variation of $\text{Pos}(C_{N,1})$ with grating angle, projecting the same signal onto different combinations of CCD pixels. Figure 10a,b plots Raman spectra and $\text{Pos}(C_{2,1})$,
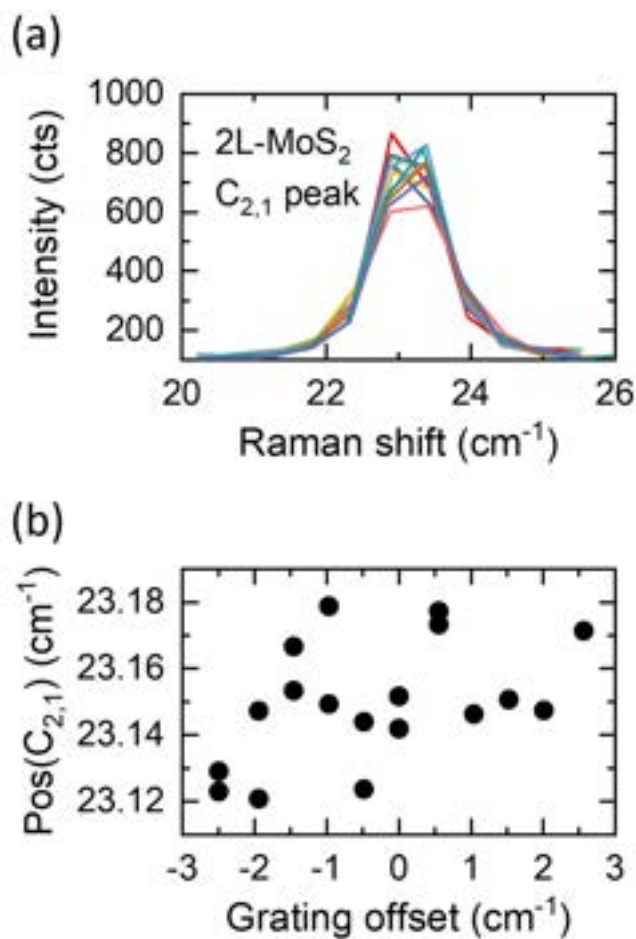
Figure 10. (a) $C_{2,1}$ for different spectrometer grating offsets. (b) $Pos(C_{2,1})$ as a function of relative grating position offsets.

Figure 11. N identification in ML-WSe$_2$. The black line is a plot of eq 1 based on $Pos(C)_\infty \sim 24.38$ cm^{-1}. Colored solid lines are $Pos(C_{N,1})$ for the ML-WSe$_2$ regions of Figure 1, with dashed lines indicating the total fitting error.

respectively, for 2L-MoS$_2$ and different grating positions, indicated by the relative offset to the first two measurements. The variation of $Pos(C_{2,1})$ has a standard deviation $\sim$0.02 cm^{-1} and a maximum $\sim$0.06 cm^{-1}. As $C_{N,1}$ peaks in regions with different N values will be detected differently, depending on the pixel registry, we use the highest of these two numbers to evaluate the fitting error.

We can now evaluate the expected error in WSe$_2$ thickness identification. Table 1 summarizes $Pos(C_{N,1})$ and the corresponding

Table 1. $Pos(C_{N,1})$ and Associated Fitting Errors in ML-WSe$_2$

region	$Pos(C_{N,1})$ (cm^{-1})	general fitting error (cm^{-1})	statistical error (cm^{-1})	subpixel fitting error (cm^{-1})	total error (cm^{-1})
1	23.76	±0.01	±0.04	±0.06	±0.06
2	24.03	±0.01	±0.01	±0.06	±0.06
bulk	24.38	±0.01	±0.01	±0.06	±0.06

errors for thickness evaluation. Figure 11 compares eq 1 (black) with the fitted $Pos(C_{N,1})$ for the ML-WSe$_2$ of Figure 1. Solid lines correspond to the mean value, and dashed lines indicate position error. We identify Region 1 as $N = 7$ and Region 2 as 10 ± 1.

Time-Resolved Photoemission Electron Microscopy. We use a high-repetition-rate, high-power Yb fiber laser (Tangerine 30, Amplitude Systemes), which delivers 40 μJ, 320 fs pulses at 0.6 MHz and a 1.03 μm center wavelength (1.20 eV photon energy). After spectral broadening in a Xe-filled hollow-core fiber,[138] a combination of highly dispersive chirped mirrors and a pair of wedges compress pulses to 50 fs FWHM duration. Second and third harmonics, with photon energies $\sim$2.41 and 3.61 eV, are generated through nonlinear frequency
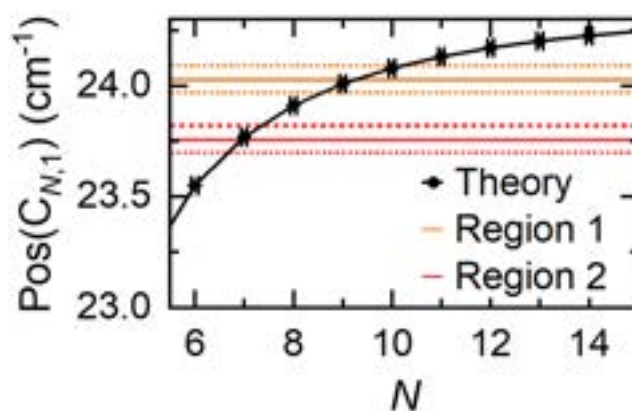
conversion in β-barium borate crystals, followed by temporal compression using a prism pair. The FWHM of the second harmonic, which acts as a pump beam, is $\sim$46 fs, whereas that of the third harmonic, acting as a probe, is $\sim$40 fs.

The pump beam is sent into a computer-controlled optical delay line to vary the time delay between the pump and probe pulses. The overall time resolution, as determined by pump−probe cross-correlation at the sample position, has FWHM $\sim$ 55 fs. The PEEM microscope (Focus GmbH, PEEM-IS) has a spatial resolution $\sim$77 nm according to the 16−84% criterion, defined as the distance over which the image intensity decreases from 84% to 16% of its maximum.[91,139] At each time delay, the image acquisition time is 19 s. Time-zero is defined as the pump−probe time delay when the peaks of the pump and probe pulse envelopes overlap. It is determined by global fitting of the PEEM signals from 1L- and 7L-WSe$_2$. This approach determines time-zero with an uncertainty <2 fs. Our measurements employ a time-integrated detector and do not resolve the dynamics of the photoemission process. Thus, the temporal behavior of secondary e emission does not contribute to the observed pump−probe dynamics.

We now consider possible artifacts associated with surface photovoltage, space-charge, and sample charging effects. Surface photovoltage and space-charge lead to shifts[140] and broadening of the photoemission spectra,[141] respectively. These do not affect energy-integrated TR-PEEM measurements, such as ours, consistent with the fact that corrections for these effects in energy-resolved measurements do not affect the total number of photoemitted e.[115,142] For a set of time delays t_i, the data acquisition program collects a PEEM image at t_i, $S(t_i)$, and immediately after that, an image at 250 ps, $S(250_i)$. The differential PEEM signal is given by $\Delta S(t_i) = S(t_i) - S(250_i)$. Since the acquisition time of individual images is 19 s, while sample charging builds up over an $\sim$1 h time scale under our conditions, sample charging is minimized by referencing to the images collected at 250 ps. As the pump−probe signal is negligible ($\sim$0.2% of the peak pump−probe signal) at this 250 ps time delay, this referencing procedure also allows for the removal of one-color multiphoton pump-only and multiphoton probe-only signals. The spatial dependence of the PEEM signal in the 7L-WSe$_2$ region, in Figure 5c and assigned to the depletion width, cannot originate from surface photovoltage, because our energy-integrated measurements are insensitive to energy shifts induced by surface photovoltage.[140]

Ab Initio Nonadiabatic Molecular Dynamics. Simulations based on nonadiabatic molecular dynamics allow us to model quantum transitions between electronic states responsible for charge transfer and recombination accompanied by e-vibrational energy relaxation. Geometry optimization, electronic structure, and adiabatic molecular dynamics simulations are performed with the Vienna *ab initio* simulation package (VASP).[143,144] The Perdew−Burke−Ernzerhof[145] functional is chosen to describe the electronic exchange-correlation energy. The projector-augmented wave[146] approach with a 400 eV

plane-wave basis energy cutoff is used to treat interactions between ionic cores and valence electrons. The van der Waals interactions are described with the Grimme DFT-D3 method.[147] The periodic images are separated by ~15 Å vacuum perpendicular to the normal of the 1L/2L WSe$_2$ plane to screen off spurious interactions. Geometry relaxation stops when the ion forces are $<10^{-3}$ eV Å^{-1}.

The nonadiabatic molecular dynamics simulation of the photo-induced charge transfer is performed using the mixed quantum-classical fewest-switches surface-hopping technique,[148] implemented within the time-dependent Kohn−Sham theory.[134,149] The e densities of edge states excluded from the simulations are given in the Supporting Information. The e−h recombination is modeled by the decoherence-induced fewest-switches surface hopping approach,[150] taking into account loss of coherence in the e subsystem induced by coupling to phonons. The decoherence time is estimated as the pure-dephasing time of the optical response using the second-order cumulant approximation.[151,152] The e densities of edge states excluded from the simulations are given in the Supporting Information. After geometry optimization, the system is heated to 300 K using uniform velocity rescaling. Then, a 6 ps adiabatic molecular dynamics trajectory is obtained with a 1 fs time step in the microcanonical ensemble. The trajectory is used to perform the nonadiabatic molecular dynamics calculations. In order to model e−h recombination over hundreds ps, the 6 ps nonadiabatic molecular dynamics Hamiltonian is iterated under the classical path approximation. Detailed information on the simulation algorithms is given in refs 153 and 154. This methodology was previously used to model excited state dynamics in a broad range of materials, such as semiconductor[155] and metallic[156] quantum dots, nanotubes,[157] metal halide perovskites,[158] plasmonic structures,[159] transition metal oxides,[160] and nanoscale interfaces.[161]

ASSOCIATED CONTENT

Ⓢ Supporting Information

The Supporting Information is available free of charge at https://pubs.acs.org/doi/10.1021/acsnano.3c06473.

> Determination of photon order and probe window, kinetic modeling of TR-PEEM, characterization and TR-PEEM time traces of isolated 1L-WSe$_2$, analysis of decay amplitudes of 1L-WSe$_2$, estimation of exciton densities of isolated 1L-WSe$_2$ and 1L−7L-WSe$_2$, extraction of depletion width and its time dependence, and charge density plots of edge states (PDF)

AUTHOR INFORMATION

Corresponding Authors

Andrea C. Ferrari − *Cambridge Graphene Centre, University of Cambridge, Cambridge CB3 0FA, U.K.;* ⓘ orcid.org/0000-0003-0907-9993; Email: acf26@eng.cam.ac.uk

Oleg V. Prezhdo − *Department of Chemistry, University of Southern California, Los Angeles, California 90089, United States;* ⓘ orcid.org/0000-0002-5140-7500; Email: prezhdo@usc.edu

Zhi-Heng Loh − *School of Chemistry, Chemical Engineering and Biotechnology, and School of Physical and Mathematical Sciences, Nanyang Technological University, Singapore 637371, Singapore;* ⓘ orcid.org/0000-0001-9729-9632; Email: zhiheng@ntu.edu.sg

Authors

Ce Xu − *School of Chemistry, Chemical Engineering and Biotechnology, and School of Physical and Mathematical Sciences, Nanyang Technological University, Singapore 637371, Singapore*

Natalie Barden − *School of Chemistry, Chemical Engineering and Biotechnology, and School of Physical and Mathematical*

Sciences, Nanyang Technological University, Singapore 637371, Singapore

Evgeny M. Alexeev − *Cambridge Graphene Centre, University of Cambridge, Cambridge CB3 0FA, U.K.;* ⓘ orcid.org/0000-0002-8149-6364

Xiaoli Wang − *College of Chemistry, Key Laboratory of Theoretical and Computational Photochemistry, Beijing Normal University, Beijing 100875, People's Republic of China*

Run Long − *College of Chemistry, Key Laboratory of Theoretical and Computational Photochemistry, Beijing Normal University, Beijing 100875, People's Republic of China;* ⓘ orcid.org/0000-0003-3912-8899

Alisson R. Cadore − *Cambridge Graphene Centre, University of Cambridge, Cambridge CB3 0FA, U.K.*

Ioannis Paradisanos − *Cambridge Graphene Centre, University of Cambridge, Cambridge CB3 0FA, U.K.;* ⓘ orcid.org/0000-0001-8310-710X

Anna K. Ott − *Cambridge Graphene Centre, University of Cambridge, Cambridge CB3 0FA, U.K.*

Giancarlo Soavi − *Cambridge Graphene Centre, University of Cambridge, Cambridge CB3 0FA, U.K.; Institute of Solid State Physics, Friedrich Schiller University Jena, 07743 Jena, Germany;* ⓘ orcid.org/0000-0003-2434-2251

Sefaattin Tongay − *School for Engineering of Matter, Transport and Energy, Arizona State University, Tempe, Arizona 85287, United States;* ⓘ orcid.org/0000-0001-8294-984X

Giulio Cerullo − *Department of Physics, Politecnico di Milano, I-20133 Milano, Italy; IFN-CNR, I-20133 Milano, Italy;* ⓘ orcid.org/0000-0002-9534-2702

Complete contact information is available at:
https://pubs.acs.org/10.1021/acsnano.3c06473

Notes

The authors declare no competing financial interest.

REFERENCES

(1) Duong, D. L.; Yun, S. J.; Lee, Y. H. Van Der Waals Layered Materials: Opportunities and Challenges. *ACS Nano* **2017**, *11* (12), 11803−11830.

(2) Bhimanapati, G. R.; Lin, Z.; Meunier, V.; Jung, Y.; Cha, J.; Das, S.; Xiao, D.; Son, Y.; Strano, M. S.; Cooper, V. R.; Liang, L.; Louie, S. G.; Ringe, E.; Zhou, W.; Kim, S. S.; Naik, R. R.; Sumpter, B. G.; Terrones, H.; Xia, F.; Wang, Y.; et al. Recent Advances in Two-Dimensional Materials Beyond Graphene. *ACS Nano* **2015**, *9* (12), 11509−11539.

(3) Jariwala, D.; Sangwan, V. K.; Lauhon, L. J.; Marks, T. J.; Hersam, M. C. Emerging Device Applications for Semiconducting Two-Dimensional Transition Metal Dichalcogenides. *ACS Nano* **2014**, *8* (2), 1102−1120.

(4) Butler, S. Z.; Hollen, S. M.; Cao, L.; Cui, Y.; Gupta, J. A.; Gutiérrez, H. R.; Heinz, T. F.; Hong, S. S.; Huang, J.; Ismach, A. F.; Johnston-Halperin, E.; Kuno, M.; Plashnitsa, V. V.; Robinson, R. D.; Ruoff, R. S.; Salahuddin, S.; Shan, J.; Shi, L.; Spencer, M. G.; Terrones, M.; et al. Progress, Challenges, and Opportunities in Two-Dimensional Materials Beyond Graphene. *ACS Nano* **2013**, *7* (4), 2898−2926.

(5) Ferrari, A. C.; Bonaccorso, F.; Fal'ko, V.; Novoselov, K. S.; Roche, S.; Bøggild, P.; Borini, S.; Koppens, F. H. L.; Palermo, V.; Pugno, N.; Garrido, J. A.; Sordan, R.; Bianco, A.; Ballerini, L.; Prato, M.; Lidorikis, E.; Kivioja, J.; Marinelli, C.; Ryhänen, T.; Morpurgo, A.; et al. Science and Technology Roadmap for Graphene, Related Two-Dimensional Crystals, and Hybrid Systems. *Nanoscale* **2015**, *7* (11), 4598−4810.

(6) Bonaccorso, F.; Sun, Z.; Hasan, T.; Ferrari, A. C. Graphene Photonics and Optoelectronics. *Nat. Photonics* **2010**, *4* (9), 611−622.

(7) Koppens, F. H. L.; Mueller, T.; Avouris, P.; Ferrari, A. C.; Vitiello, M. S.; Polini, M. Photodetectors Based on Graphene, Other Two-Dimensional Materials and Hybrid Systems. *Nat. Nanotechnol.* **2014**, *9* (10), 780−793.

(8) Zhao, W.; Ghorannevis, Z.; Chu, L.; Toh, M.; Kloc, C.; Tan, P.-H.; Eda, G. Evolution of Electronic Structure in Atomically Thin Sheets of WS_2 and WSe_2. *ACS Nano* **2013**, *7* (1), 791−797.

(9) Zhang, Y.; Chang, T.-R.; Zhou, B.; Cui, Y.-T.; Yan, H.; Liu, Z.; Schmitt, F.; Lee, J.; Moore, R.; Chen, Y.; et al. Direct Observation of the Transition from Indirect to Direct Bandgap in Atomically Thin Epitaxial $MoSe_2$. *Nat. Nanotechnol.* **2014**, *9* (2), 111.

(10) Rezende, N. P.; Cadore, A. R.; Gadelha, A. C.; Pereira, C. L.; Ornelas, V.; Watanabe, K.; Taniguchi, T.; Ferlauto, A. S.; Malachias, A.; Campos, L. C.; Lacerda, R. G. Probing the Electronic Properties of Monolayer MoS_2 Via Interaction with Molecular Hydrogen. *Adv. Electron. Mater.* **2019**, *5* (2), 1800591.

(11) Radisavljevic, B.; Radenovic, A.; Brivio, J.; Giacometti, V.; Kis, A. Single-Layer MoS_2 Transistors. *Nat. Nanotechnol.* **2011**, *6* (3), 147−150.

(12) Radisavljevic, B.; Kis, A. Mobility Engineering and a Metal−Insulator Transition in Monolayer MoS_2. *Nat. Mater.* **2013**, *12* (9), 815−820.

(13) Kang, K.; Xie, S.; Huang, L.; Han, Y.; Huang, P. Y.; Mak, K. F.; Kim, C.-J.; Muller, D.; Park, J. High-Mobility Three-Atom-Thick Semiconducting Films with Wafer-Scale Homogeneity. *Nature* **2015**, *520* (7549), 656−660.

(14) Piatti, E.; Fazio, De; Daghero, D.; Tamalampudi, D.; Yoon, S. R.; Ferrari, D.; Gonnelli, A. C.; Multi-Valley, R. S. Superconductivity in Ion-Gated MoS_2 Layers. *Nano Lett.* **2018**, *18* (8), 4821−4830.

(15) Orchin, G. J.; De Fazio, D.; Di Bernardo, A.; Hamer, M.; Yoon, D.; Cadore, A. R.; Goykhman, I.; Watanabe, K.; Taniguchi, T.; Robinson, J. W.; et al. Niobium Diselenide Superconducting Photodetectors. *Appl. Phys. Lett.* **2019**, *114* (25), 251103.

(16) Barbone, M.; Montblanch, A. R. P.; Kara, D. M.; Palacios-Berraquero, C.; Cadore, A. R.; De Fazio, D.; Pingault, B.; Mostaani, E.; Li, H.; Chen, B.; Watanabe, K.; Taniguchi, T.; Tongay, S.; Wang, G.; Ferrari, A. C.; Atatüre, M. Charge-Tuneable Biexciton Complexes in Monolayer WSe_2. *Nat. Commun.* **2018**, *9* (1), 3721.

(17) Chernikov, A.; Berkelbach, T. C.; Hill, H. M.; Rigosi, A.; Li, Y.; Aslan, O. B.; Reichman, D. R.; Hybertsen, M. S.; Heinz, T. F. Exciton Binding Energy and Nonhydrogenic Rydberg Series in Monolayer WS_2. *Phys. Rev. Lett.* **2014**, *113* (7), 076802.

(18) Bellus, M. Z.; Ceballos, F.; Chiu, H.-Y.; Zhao, H. Tightly Bound Trions in Transition Metal Dichalcogenide Heterostructures. *ACS Nano* **2015**, *9* (6), 6459−6464.

(19) Mostaani, E.; Szyniszewski, M.; Price, C. H.; Maezono, R.; Danovich, M.; Hunt, R. J.; Drummond, N. D.; Fal'ko, V. I. Diffusion Quantum Monte Carlo Study of Excitonic Complexes in Two-Dimensional Transition-Metal Dichalcogenides. *Phys. Rev. B* **2017**, *96* (7), No. 075431.

(20) Klimmer, S.; Ghaebi, O.; Gan, Z.; George, A.; Turchanin, A.; Cerullo, G.; Soavi, G. All-Optical Polarization and Amplitude Modulation of Second-Harmonic Generation in Atomically Thin Semiconductors. *Nat. Photonics* **2021**, *15* (11), 837−842.

(21) Soavi, G.; Wang, G.; Rostami, H.; Purdie, D. G.; De Fazio, D.; Ma, T.; Luo, B.; Wang, J.; Ott, A. K.; Yoon, D.; Bourelle, S. A.; Muench, J. E.; Goykhman, I.; Dal Conte, S.; Celebrano, M.; Tomadin, A.; Polini, M.; Cerullo, G.; Ferrari, A. C. Broadband, Electrically Tunable Third-Harmonic Generation in Graphene. *Nat. Nanotechnol.* **2018**, *13* (7), 583−588.

(22) Bikorimana, S.; Lama, P.; Walser, A.; Dorsinville, R.; Anghel, S.; Mitioglu, A.; Micu, A.; Kulyuk, L. Nonlinear Optical Responses in Two-Dimensional Transition Metal Dichalcogenide Multilayer: WS_2, WSe_2, MoS_2 and $Mo_{0.5}w_{0.5}s_2$. *Opt. Express* **2016**, *24* (18), 20685−20695.

(23) Säynätjoki, A.; Karvonen, L.; Rostami, H.; Autere, A.; Mehravar, S.; Lombardo, A.; Norwood, R. A.; Hasan, T.; Peyghambarian, N.; Lipsanen, H.; Kieu, K.; Ferrari, A. C.; Polini, M.; Sun, Z. Ultra-Strong Nonlinear Optical Processes and Trigonal Warping in MoS_2 Layers. *Nat. Commun.* **2017**, *8* (1), 893.

(24) Lafeta, L.; Corradi, A.; Zhang, T.; Kahn, E.; Bilgin, I.; Carvalho, B. R.; Kar, S.; Terrones, M.; Malard, L. M. Second- and Third-Order Optical Susceptibilities across Excitons States in 2D Monolayer Transition Metal Dichalcogenides. *2D Mater.* **2021**, *8* (3), 035010.

(25) Scarpelli, L.; Masia, F.; Alexeev, E. M.; Withers, F.; Tartakovskii, A. I.; Novoselov, K. S.; Langbein, W. Resonantly Excited Exciton Dynamics in Two-Dimensional $MoSe_2$ Monolayers. *Phys. Rev. B* **2017**, *96* (4), No. 045407.

(26) Wang, G.; Chernikov, A.; Glazov, M. M.; Heinz, T. F.; Marie, X.; Amand, T.; Urbaszek, B. Colloquium: Excitons in Atomically Thin Transition Metal Dichalcogenides. *Rev. Mod. Phys.* **2018**, *90* (2), 021001.

(27) Trovatello, C.; Miranda, H. P. C.; Molina-Sánchez, A.; Borrego-Varillas, R.; Manzoni, C.; Moretti, L.; Ganzer, L.; Maiuri, M.; Wang, J.; Dumcenco, D.; Kis, A.; Wirtz, L.; Marini, A.; Soavi, G.; Ferrari, A. C.; Cerullo, G.; Sangalli, D.; Conte, S. D. Strongly Coupled Coherent Phonons in Single-Layer MoS_2. *ACS Nano* **2020**, *14* (5), 5700−5710.

(28) Paradisanos, I.; Wang, G.; Alexeev, E. M.; Cadore, A. R.; Marie, X.; Ferrari, A. C.; Glazov, M. M.; Urbaszek, B. Efficient Phonon Cascades in WSe_2 Monolayers. *Nat. Commun.* **2021**, *12* (1), 538.

(29) Li, D.; Trovatello, C.; Dal Conte, S.; Nuß, M.; Soavi, G.; Wang, G.; Ferrari, A. C.; Cerullo, G.; Brixner, T. Exciton−Phonon Coupling Strength in Single-Layer $MoSe_2$ at Room Temperature. *Nat. Commun.* **2021**, *12* (1), 954.

(30) Bonaccorso, F.; Lombardo, A.; Hasan, T.; Sun, Z.; Ferrari, A. C. Production and Processing of Graphene and 2D Crystals. *Mater. Today* **2012**, *15* (12), 564−589.

(31) Choi, W.; Choudhary, N.; Gang, H. H.; Park, J.; Akinwande, D.; Lee, Y. H. Recent Development of Two-Dimensional Transition Metal Dichalcogenides and Their Applications. *Mater. Today* **2017**, *20* (3), 116−130.

(32) Backes, C.; Abdelkader, A. M.; Alonso, C.; Andrieux-Ledier, A.; Arenal, R.; Azpeitia, J.; Balakrishnan, N.; Banszerus, L.; Barjon, J.; Bartali, R.; Bellani, S.; Berger, C.; Berger, R.; Ortega, M. M. B.; Bernard, C.; Beton, P. H.; Beyer, A.; Bianco, A.; Bøggild, P.; Bonaccorso, F.; et al. Production and Processing of Graphene and Related Materials. *2D Mater.* **2020**, *7* (2), 022001.

(33) De Fazio, D.; Goykhman, I.; Yoon, D.; Bruna, M.; Eiden, A.; Milana, S.; Sassi, U.; Barbone, M.; Dumcenco, D.; Marinov, K.; Kis, A.; Ferrari, A. C. High Responsivity, Large-Area Graphene/MoS_2 Flexible Photodetectors. *ACS Nano* **2016**, *10* (9), 8252−8262.

(34) Huo, N.; Konstantatos, G. Ultrasensitive All-2D MoS_2 Phototransistors Enabled by an out-of-Plane MoS_2 Pn Homojunction. *Nat. Commun.* **2017**, *8* (1), 572.

(35) Gadelha, A. C.; Cadore, A. R.; Watanabe, K.; Taniguchi, T.; de Paula, A. M.; Malard, L. M.; Lacerda, R. G.; Campos, L. C. Gate-Tunable Non-Volatile Photomemory Effect in MoS_2 Transistors. *2D Mater.* **2019**, *6* (2), 025036.

(36) Sundaram, R.; Engel, M.; Lombardo, A.; Krupke, R.; Ferrari, A.; Avouris, P.; Steiner, M. Electroluminescence in Single Layer MoS_2. *Nano Lett.* **2013**, *13* (4), 1416−1421.

(37) Palacios-Berraquero, C.; Barbone, M.; Kara, D. M.; Chen, X.; Goykhman, I.; Yoon, D.; Ott, A. K.; Beitner, J.; Watanabe, K.;

Taniguchi, T.; Ferrari, A. C.; Atatüre, M. Atomically Thin Quantum Light-Emitting Diodes. *Nat. Commun.* **2016**, *7* (1), 12978.

(38) Wang, J.; Verzhbitskiy, I.; Eda, G. Electroluminescent Devices Based on 2D Semiconducting Transition Metal Dichalcogenides. *Adv. Mater.* **2018**, *30* (47), 1802687.

(39) Peña Román, R. J.; Auad, Y.; Grasso, L.; Alvarez, F.; Barcelos, I. D.; Zagonel, L. F. Tunneling-Current-Induced Local Excitonic Luminescence in p-Doped WSe2 Monolayers. *Nanoscale* **2020**, *12* (25), 13460−13470.

(40) Manzeli, S.; Ovchinnikov, D.; Pasquier, D.; Yazyev, O. V.; Kis, A. 2D Transition Metal Dichalcogenides. *Nat. Rev. Mater.* **2017**, *2* (8), 17033.

(41) Zhang, X.-Q.; Lin, C.-H.; Tseng, Y.-W.; Huang, K.-H.; Lee, Y.-H. Synthesis of Lateral Heterostructures of Semiconducting Atomic Layers. *Nano Lett.* **2015**, *15* (1), 410−415.

(42) Liu, Y.; Weiss, N. O.; Duan, X.; Cheng, H.-C.; Huang, Y.; Duan, X. Van Der Waals Heterostructures and Devices. *Nat. Rev. Mater.* **2016**, *1* (9), 1−17.

(43) Shinde, S. M.; Dhakal, K. P.; Chen, X.; Yun, W. S.; Lee, J.; Kim, H.; Ahn, J.-H. Stacking-Controllable Interlayer Coupling and Symmetric Configuration of Multilayered MoS2. *NPG Asia Materials* **2018**, *10* (2), e468−e468.

(44) Sahoo, P. K.; Memaran, S.; Xin, Y.; Balicas, L.; Gutiérrez, H. R. One-Pot Growth of Two-Dimensional Lateral Heterostructures Via Sequential Edge-Epitaxy. *Nature* **2018**, *553* (7686), 63−67.

(45) Komsa, H.-P.; Krasheninnikov, A. V. Electronic Structures and Optical Properties of Realistic Transition Metal Dichalcogenide Heterostructures from First Principles. *Phys. Rev. B* **2013**, *88* (8), No. 085318.

(46) Gong, Y.; Lei, S.; Ye, G.; Li, B.; He, Y.; Keyshar, K.; Zhang, X.; Wang, Q.; Lou, J.; Liu, Z.; et al. Two-Step Growth of Two-Dimensional WSe2/MoSe2 Heterostructures. *Nano Lett.* **2015**, *15* (9), 6135−6141.

(47) Furchi, M. M.; Pospischil, A.; Libisch, F.; Burgdörfer, J.; Mueller, T. Photovoltaic Effect in an Electrically Tunable Van Der Waals Heterojunction. *Nano Lett.* **2014**, *14* (8), 4785−4791.

(48) Sahoo, P. K.; Memaran, S.; Nugera, F. A.; Xin, Y.; Díaz Márquez, T.; Lu, Z.; Zheng, W.; Zhigadlo, N. D.; Smirnov, D.; Balicas, L.; Gutiérrez, H. R. Bilayer Lateral Heterostructures of Transition-Metal Dichalcogenides and Their Optoelectronic Response. *ACS Nano* **2019**, *13* (11), 12372−12384.

(49) Huo, N.; Kang, J.; Wei, Z.; Li, S.-S.; Li, J.; Wei, S.-H. Novel and Enhanced Optoelectronic Performances of Multilayer MoS2−WS2 Heterostructure Transistors. *Adv. Funct. Mater.* **2014**, *24* (44), 7025−7031.

(50) Huo, N.; Tongay, S.; Guo, W.; Li, R.; Fan, C.; Lu, F.; Yang, J.; Li, B.; Li, Y.; Wei, Z. Novel Optical and Electrical Transport Properties in Atomically Thin WSe2/MoS2 p−n Heterostructures. *Adv. Electron. Mater.* **2015**, *1* (5), 1400066.

(51) Jauregui, L. A.; Joe, A. Y.; Pistunova, K.; Wild, D. S.; High, A. A.; Zhou, Y.; Scuri, G.; De Greve, K.; Sushko, A.; Yu, C.-H.; Taniguchi, T.; Watanabe, K.; Needleman, D. J.; Lukin, M. D.; Park, H.; Kim, P. Electrical Control of Interlayer Exciton Dynamics in Atomically Thin Heterostructures. *Science* **2019**, *366* (6467), 870−875.

(52) Ruiz-Tijerina, D. A.; Fal'ko, V. I. Interlayer Hybridization and Moiré Superlattice Minibands for Electrons and Excitons in Heterobilayers of Transition-Metal Dichalcogenides. *Phys. Rev. B* **2019**, *99* (12), No. 125424.

(53) Alexeev, E. M.; Ruiz-Tijerina, D. A.; Danovich, M.; Hamer, M. J.; Terry, D. J.; Nayak, P. K.; Ahn, S.; Pak, S.; Lee, J.; Sohn, J. I.; Molas, M. R.; Koperski, M.; Watanabe, K.; Taniguchi, T.; Novoselov, K. S.; Gorbachev, R. V.; Shin, H. S.; Fal'ko, V. I.; Tartakovskii, A. I. Resonantly Hybridized Excitons in Moiré Superlattices in Van Der Waals Heterostructures. *Nature* **2019**, *567* (7746), 81−86.

(54) Montblanch, A. R. P.; Kara, D. M.; Paradisanos, I.; Purser, C. M.; Feuer, M. S. G.; Alexeev, E. M.; Stefan, L.; Qin, Y.; Blei, M.; Wang, G.; Cadore, A. R.; Latawiec, P.; Lončar, M.; Tongay, S.; Ferrari, A. C.; Atatüre, M. Confinement of Long-Lived Interlayer Excitons in WS2/WSe2 Heterostructures. *Commun. Phys.* **2021**, *4* (1), 119.

(55) Paradisanos, I.; Shree, S.; George, A.; Leisgang, N.; Robert, C.; Watanabe, K.; Taniguchi, T.; Warburton, R. J.; Turchanin, A.; Marie, X.; Gerber, I. C.; Urbaszek, B. Controlling Interlayer Excitons in MoS2 Layers Grown by Chemical Vapor Deposition. *Nat. Commun.* **2020**, *11* (1), 2391.

(56) Gong, C.; Zhang, H.; Wang, W.; Colombo, L.; Wallace, R. M.; Cho, K. Band Alignment of Two-Dimensional Transition Metal Dichalcogenides: Application in Tunnel Field Effect Transistors. *Appl. Phys. Lett.* **2013**, *103* (5), 053513.

(57) Chiu, M.-H.; Zhang, C.; Shiu, H.-W.; Chuu, C.-P.; Chen, C.-H.; Chang, C.-Y. S.; Chen, C.-H.; Chou, M.-Y.; Shih, C.-K.; Li, L.-J. Determination of Band Alignment in the Single-Layer MoS2/WSe2 Heterojunction. *Nat. Commun.* **2015**, *6*, 7666.

(58) Guo, Y.; Robertson, J. Band Engineering in Transition Metal Dichalcogenides: Stacked Versus Lateral Heterostructures. *Appl. Phys. Lett.* **2016**, *108* (23), 233104.

(59) Bellus, M. Z.; Li, M.; Lane, S. D.; Ceballos, F.; Cui, Q.; Zeng, X. C.; Zhao, H. Type-I Van Der Waals Heterostructure Formed by MoS2 and Res2 Monolayers. *Nanoscale Horiz.* **2017**, *2* (1), 31−36.

(60) Ross, J. S.; Rivera, P.; Schaibley, J.; Lee-Wong, E.; Yu, H.; Taniguchi, T.; Watanabe, K.; Yan, J.; Mandrus, D.; Cobden, D.; et al. Interlayer Exciton Optoelectronics in a 2D Heterostructure p−n Junction. *Nano Lett.* **2017**, *17* (2), 638−643.

(61) Ceballos, F.; Bellus, M. Z.; Chiu, H.-Y.; Zhao, H. Ultrafast Charge Separation and Indirect Exciton Formation in a MoS2−MoSe2 Van Der Waals Heterostructure. *ACS Nano* **2014**, *8* (12), 12717−12724.

(62) Hong, X.; Kim, J.; Shi, S.-F.; Zhang, Y.; Jin, C.; Sun, Y.; Tongay, S.; Wu, J.; Zhang, Y.; Wang, F. Ultrafast Charge Transfer in Atomically Thin MoS2/WS2 Heterostructures. *Nat. Nanotechnol.* **2014**, *9* (9), 682−686.

(63) Chen, H.; Wen, X.; Zhang, J.; Wu, T.; Gong, Y.; Zhang, X.; Yuan, J.; Yi, C.; Lou, J.; Ajayan, P. M.; Zhuang, W.; Zhang, G.; Zheng, J. Ultrafast Formation of Interlayer Hot Excitons in Atomically Thin MoS2/WS2 Heterostructures. *Nat. Commun.* **2016**, *7*, 12512.

(64) Zhu, H. M.; Wang, J.; Gong, Z. Z.; Kim, Y. D.; Hone, J.; Zhu, X. Y. Interfacial Charge Transfer Circumventing Momentum Mismatch at Two-Dimensional Van Der Waals Heterojunctions. *Nano Lett.* **2017**, *17* (6), 3591−3598.

(65) Ji, Z. H.; Hong, H.; Zhang, J.; Zhang, Q.; Huang, W.; Cao, T.; Qiao, R. X.; Liu, C.; Liang, J.; Jin, C. H.; Jiao, L. Y.; Shi, K. B.; Meng, S.; Liu, K. H. Robust Stacking-Independent Ultrafast Charge Transfer in MoS2/WS2 Bilayers. *ACS Nano* **2017**, *11* (12), 12020−12026.

(66) Jin, C. H.; Ma, E. Y.; Karni, O.; Regan, E. C.; Wang, F.; Heinz, T. F. Ultrafast Dynamics in Van Der Waals Heterostructures. *Nat. Nanotechnol.* **2018**, *13* (11), 994−1003.

(67) Zhou, H. Z.; Zhao, Y. D.; Zhu, H. M. Dielectric Environment-Robust Ultrafast Charge Transfer between Two Atomic Layers. *J. Phys. Chem. Lett.* **2019**, *10* (2), 150−155.

(68) Long, R.; Prezhdo, O. V. Quantum Coherence Facilitates Efficient Charge Separation at a MoS2/MoSe2 Van Der Waals Junction. *Nano Lett.* **2016**, *16* (3), 1996−2003.

(69) Wang, Y.; Wang, Z.; Yao, W.; Liu, G.-B.; Yu, H. Interlayer Coupling in Commensurate and Incommensurate Bilayer Structures of Transition-Metal Dichalcogenides. *Phys. Rev. B* **2017**, *95* (11), No. 115429.

(70) Bellus, M. Z.; Mahjouri-Samani, M.; Lane, S. D.; Oyedele, A. D.; Li, X.; Puretzky, A. A.; Geohegan, D.; Xiao, K.; Zhao, H. Photocarrier Transfer across Monolayer MoS2−MoSe2 Lateral Heterojunctions. *ACS Nano* **2018**, *12* (7), 7086−7092.

(71) Hao, H.; Xu, Z.; Jiang, T.; Wei, K.; Li, H.; Zheng, X.; Yin, K.; You, J.; Shen, C.; Cheng, X.-a. Visualized Charge Transfer Processes in Monolayer Composition-Graded Ws2xse2(1−X) Lateral Heterojunctions Via Ultrafast Microscopy Mapping. *Opt. Express* **2018**, *26* (12), 15867−15886.

(72) Howell, S. L.; Jariwala, D.; Wu, C.-C.; Chen, K.-S.; Sangwan, V. K.; Kang, J.; Marks, T. J.; Hersam, M. C.; Lauhon, L. J. Investigation of Band-Offsets at Monolayer−Multilayer MoS2 Junctions by Scanning Photocurrent Microscopy. *Nano Lett.* **2015**, *15* (4), 2278−2284.

(73) Xu, Z.-Q.; Zhang, Y.; Wang, Z.; Shen, Y.; Huang, W.; Xia, X.; Yu, W.; Xue, Y.; Sun, L.; Zheng, C.; Lu, Y.; Liao, L.; Bao, Q. Atomically Thin Lateral p−n Junction Photodetector with Large Effective Detection Area. *2D Mater.* **2016**, *3* (4), 041001.

(74) Sun, M.; Xie, D.; Sun, Y.; Li, W.; Teng, C.; Xu, J. Lateral Multilayer/Monolayer MoS₂ Heterojunction for High Performance Photodetector Applications. *Sci. Rep.* **2017**, *7* (1), 4505.

(75) Xia, C.; Xiong, W.; Du, J.; Wang, T.; Peng, Y.; Wei, Z.; Li, J.; Jia, Y. Type-I Transition Metal Dichalcogenides Lateral Homojunctions: Layer Thickness and External Electric Field Effects. *Small* **2018**, *14* (21), No. e1800365.

(76) Jia, Z.; Shi, J.; Shang, Q.; Du, W.; Shan, X.; Ge, B.; Li, J.; Sui, X.; Zhong, Y.; Wang, Q.; Bao, L.; Zhang, Q.; Liu, X. Charge-Transfer-Induced Photoluminescence Properties of WSe₂ Monolayer−Bilayer Homojunction. *ACS Appl. Mater. Interfaces* **2019**, *11* (22), 20566−20573.

(77) Wu, J. J.; Peng, J.; Zhou, Y.; Lin, Y.; Wen, X. L.; Wu, J. C.; Zhao, Y. C.; Guo, Y. Q.; Wu, C. Z.; Xie, Y. Solution Processing for Lateral Transition-Metal Dichalcogenides Homojunction from Polymorphic Crystal. *J. Am. Chem. Soc.* **2019**, *141* (1), 592−598.

(78) Wu, G. J.; Tian, B. B.; Liu, L.; Lv, W.; Wu, S.; Wang, X. D.; Chen, Y.; Li, J. Y.; Wang, Z.; Wu, S. Q.; Shen, H.; Lin, T.; Zhou, P.; Liu, Q.; Duan, C. G.; Zhang, S. T.; Meng, X. J.; Wu, S. W.; Hu, W. D.; Wang, X. R.; et al. Programmable Transition Metal Dichalcogenide Homojunctions Controlled by Nonvolatile Ferroelectric Domains. *Nat. Electron.* **2020**, *3* (1), 43−50.

(79) Utama, M. I. B.; Kleemann, H.; Zhao, W. Y.; Ong, C. S.; da Jornada, F. H.; Qiu, D. Y.; Cai, H.; Li, H.; Kou, R.; Zhao, S. H.; Wang, S.; Watanabe, K.; Taniguchi, T.; Tongay, S.; Zettl, A.; Louie, S. G.; Wang, F. A Dielectric-Defined Lateral Heterojunction in a Monolayer Semiconductor. *Nat. Electron.* **2019**, *2* (2), 60−65.

(80) Zhang, C.; Chen, Y.; Huang, J.-K.; Wu, X.; Li, L.-J.; Yao, W.; Tersoff, J.; Shih, C.-K. Visualizing Band Offsets and Edge States in Bilayer−Monolayer Transition Metal Dichalcogenides Lateral Heterojunction. *Nat. Commun.* **2016**, *7*, 10349.

(81) Fang, L.; Yuan, X.; Liu, K.; Li, L.; Zhou, P.; Ma, W.; Huang, H.; He, J.; Tao, S. Direct Bilayer Growth: A New Growth Principle for a Novel WSe₂ Homo-Junction and Bilayer WSe₂ Growth. *Nanoscale* **2020**, *12* (6), 3715−3722.

(82) Mak, K. F.; Lee, C.; Hone, J.; Shan, J.; Heinz, T. F. Atomically Thin MoS₂: A New Direct-Gap Semiconductor. *Phys. Rev. Lett.* **2010**, *105* (13), 136805.

(83) Splendiani, A.; Sun, L.; Zhang, Y.; Li, T.; Kim, J.; Chim, C.-Y.; Galli, G.; Wang, F. Emerging Photoluminescence in Monolayer MoS₂. *Nano Lett.* **2010**, *10* (4), 1271−1275.

(84) Zeng, H.; Liu, G.-B.; Dai, J.; Yan, Y.; Zhu, B.; He, R.; Xie, L.; Xu, S.; Chen, X.; Yao, W.; et al. Optical Signature of Symmetry Variations and Spin-Valley Coupling in Atomically Thin Tungsten Dichalcogenides. *Sci. Rep.* **2013**, *3*, 1608.

(85) Tosun, M.; Fu, D. Y.; Desai, S. B.; Ko, C.; Kang, J. S.; Lien, D. H.; Najmzadeh, M.; Tongay, S.; Wu, J. Q.; Javey, A. MoS₂ Heterojunctions by Thickness Modulation. *Sci. Rep.* **2015**, *5*, 10990.

(86) Novoselov, K. S.; Jiang, D.; Schedin, F.; Booth, T. J.; Khotkevich, V. V.; Morozov, S. V.; Geim, A. K. Two-Dimensional Atomic Crystals. *Proc. Natl. Acad. Sci. U.S.A.* **2005**, *102* (30), 10451−10453.

(87) Jarrett, J. W.; Zhao, T.; Johnson, J. S.; Knappenberger, K. L. Investigating Plasmonic Structure-Dependent Light Amplification and Electronic Dynamics Using Advances in Nonlinear Optical Microscopy. *J. Phys. Chem. C* **2015**, *119* (28), 15779−15800.

(88) Beane, G.; Devkota, T.; Brown, B. S.; Hartland, G. V. Ultrafast Measurements of the Dynamics of Single Nanostructures: A Review. *Rep. Prog. Phys.* **2019**, *82* (1), 016401.

(89) Zhu, T.; Snaider, J. M.; Yuan, L.; Huang, L. Ultrafast Dynamic Microscopy of Carrier and Exciton Transport. *Annu. Rev. Phys. Chem.* **2019**, *70* (1), 219−244.

(90) Fukumoto, K.; Onda, K.; Yamada, Y.; Matsuki, T.; Mukuta, T.; Tanaka, S.-i.; Koshihara, S.-y. Femtosecond Time-Resolved Photoemission Electron Microscopy for Spatiotemporal Imaging of Photo-

generated Carrier Dynamics in Semiconductors. *Rev. Sci. Instrum.* **2014**, *85* (8), 083705.

(91) Doherty, T. A. S.; Winchester, A. J.; Macpherson, S.; Johnstone, D. N.; Pareek, V.; Tennyson, E. M.; Kosar, S.; Kosasih, F. U.; Anaya, M.; Abdi-Jalebi, M.; Andaji-Garmaroudi, Z.; Wong, E. L.; Madéo, J.; Chiang, Y.-H.; Park, J.-S.; Jung, Y.-K.; Petoukhoff, C. E.; Divitini, G.; Man, M. K. L.; Ducati, C.; et al. Performance-Limiting Nanoscale Trap Clusters at Grain Junctions in Halide Perovskites. *Nature* **2020**, *580* (7803), 360−366.

(92) Fukumoto, K.; Yamada, Y.; Onda, K.; Koshihara, S.-y. Direct Imaging of Electron Recombination and Transport on a Semiconductor Surface by Femtosecond Time-Resolved Photoemission Electron Microscopy. *Appl. Phys. Lett.* **2014**, *104* (5), 053117.

(93) Man, M. K.; Margiolakis, A.; Deckoff-Jones, S.; Harada, T.; Wong, E. L.; Krishna, M. B. M.; Madéo, J.; Winchester, A.; Lei, S.; Vajtai, R.; et al. Imaging the Motion of Electrons across Semiconductor Heterojunctions. *Nat. Nanotechnol.* **2017**, *12* (1), 36.

(94) Wang, L.; Xu, C.; Li, M. Y.; Li, L. J.; Loh, Z.-H. Unraveling Spatially Heterogeneous Ultrafast Carrier Dynamics of Single-Layer WSe₂ by Femtosecond Time-Resolved Photoemission Electron Microscopy. *Nano Lett.* **2018**, *18* (8), 5172−5178.

(95) Xu, C.; Yong, H. W.; He, J.; Long, R.; Cadore, A. R.; Paradisanos, I.; Ott, A. K.; Soavi, G.; Tongay, S.; Cerullo, G.; Ferrari, A. C.; Prezhdo, O. V.; Loh, Z.-H. Weak Distance Dependence of Hot-Electron-Transfer Rates at the Interface between Monolayer MoS₂ and Gold. *ACS Nano* **2021**, *15* (1), 819−828.

(96) Castellanos-Gomez, A.; Buscema, M.; Molenaar, R.; Singh, V.; Janssen, L.; van der Zant, H. S. J.; Steele, G. A. Deterministic Transfer of Two-Dimensional Materials by All-Dry Viscoelastic Stamping. *2D Mater.* **2014**, *1* (1), 011002.

(97) Casiraghi, C.; Hartschuh, A.; Lidorikis, E.; Qian, H.; Harutyunyan, H.; Gokus, T.; Novoselov, K. S.; Ferrari, A. C. Rayleigh Imaging of Graphene and Graphene Layers. *Nano Lett.* **2007**, *7* (9), 2711−2717.

(98) Ferrari, A. C.; Basko, D. M. Raman Spectroscopy as a Versatile Tool for Studying the Properties of Graphene. *Nat. Nanotechnol.* **2013**, *8* (4), 235−246.

(99) Tan, P. H.; Han, W. P.; Zhao, W. J.; Wu, Z. H.; Chang, K.; Wang, H.; Wang, Y. F.; Bonini, N.; Marzari, N.; Pugno, N.; Savini, G.; Lombardo, A.; Ferrari, A. C. The Shear Mode of Multilayer Graphene. *Nat. Mater.* **2012**, *11* (4), 294−300.

(100) Zhang, X.; Han, W. P.; Wu, J. B.; Milana, S.; Lu, Y.; Li, Q. Q.; Ferrari, A. C.; Tan, P. H. Raman Spectroscopy of Shear and Layer Breathing Modes in Multilayer MoS₂. *Phys. Rev. B* **2013**, *87* (11), No. 115413.

(101) Pizzi, G.; Milana, S.; Ferrari, A. C.; Marzari, N.; Gibertini, M. Shear and Breathing Modes of Layered Materials. *ACS Nano* **2021**, *15* (8), 12509−12534.

(102) Molas, M. R.; Tyurnina, A. V.; Zólyomi, V.; Ott, A. K.; Terry, D. J.; Hamer, M. J.; Yelgel, C.; Babiński, A.; Nasibulin, A. G.; Ferrari, A. C.; Fal'ko, V. I.; Gorbachev, R. Raman Spectroscopy of Gase and Inse Post-Transition Metal Chalcogenides Layers. *Faraday Discuss.* **2021**, *227* (0), 163−170.

(103) Zhao, W.; Ghorannevis, Z.; Amara, K. K.; Pang, J. R.; Toh, M.; Zhang, X.; Kloc, C.; Tan, P. H.; Eda, G. Lattice Dynamics in Mono- and Few-Layer Sheets of WS₂ and WSe₂. *Nanoscale* **2013**, *5* (20), 9677−9683.

(104) Terrones, H.; Corro, E. D.; Feng, S.; Poumirol, J. M.; Rhodes, D.; Smirnov, D.; Pradhan, N. R.; Lin, Z.; Nguyen, M. A. T.; Elías, A. L.; Mallouk, T. E.; Balicas, L.; Pimenta, M. A.; Terrones, M. New First Order Raman-Active Modes in Few Layered Transition Metal Dichalcogenides. *Sci. Rep.* **2014**, *4* (1), 4215.

(105) del Corro, E.; Terrones, H.; Elias, A.; Fantini, C.; Feng, S.; Nguyen, M. A.; Mallouk, T. E.; Terrones, M.; Pimenta, M. A. Excited Excitonic States in 1L, 2L, 3L, and Bulk WSe₂ Observed by Resonant Raman Spectroscopy. *ACS Nano* **2014**, *8* (9), 9629−9635.

(106) Shi, W.; Lin, M.-L.; Tan, Q.-H.; Qiao, X.-F.; Zhang, J.; Tan, P.-H. Raman and Photoluminescence Spectra of Two-Dimensional

Nanocrystallites of Monolayer WS_2 and WSe_2. *2D Mater.* **2016**, *3* (2), 025016.

(107) dos Santos, E. P.; Silva, F. L. R.; Gontijo, R. N.; Alves, J. M.; Ammar, M.-R; Fantini, C. Temperature Dependence of the Double-Resonance Raman Bands in Bilayer WSe_2. *Vib. Spectrosc* **2020**, *110*, No. 103117.

(108) Huang, W.; Luo, X.; Gan, C. K.; Quek, S. Y.; Liang, G. Theoretical Study of Thermoelectric Properties of Few-Layer MoS_2 and WSe_2. *Phys. Chem. Chem. Phys.* **2014**, *16* (22), 10866−10874.

(109) Kim, H.-g.; Choi, H. J. Thickness Dependence of Work Function, Ionization Energy, and Electron Affinity of Mo and W Dichalcogenides from DFT and GW Calculations. *Phys. Rev. B* **2021**, *103* (8), No. 085404.

(110) Nie, Z.; Long, R.; Sun, L.; Huang, C.-C.; Zhang, J.; Xiong, Q.; Hewak, D. W.; Shen, Z.; Prezhdo, O. V.; Loh, Z.-H. Ultrafast Carrier Thermalization and Cooling Dynamics in Few-Layer MoS_2. *ACS Nano* **2014**, *8* (10), 10931−10940.

(111) Li, A.; James, N. A.; Wang, T.; Wang, Z.; Petek, H.; Reutzel, M. Towards Full Surface Brillouin Zone Mapping by Coherent Multi-Photon Photoemission. *New J. Phys.* **2020**, *22* (7), 073035.

(112) Hüfner, S. *Photoelectron Spectroscopy: Principles and Applications*, 3rd ed.; Springer-Verlag: 2003.

(113) Keyshar, K.; Berg, M.; Zhang, X.; Vajtai, R.; Gupta, G.; Chan, C. K.; Beechem, T. E.; Ajayan, P. M.; Mohite, A. D.; Ohta, T. Experimental Determination of the Ionization Energies of $MoSe_2$, WS_2, and MoS_2 on SiO_2 Using Photoemission Electron Microscopy. *ACS Nano* **2017**, *11* (8), 8223−8230.

(114) Wallauer, R.; Perea-Causin, R.; Münster, L.; Zajusch, S.; Brem, S.; Güdde, J.; Tanimura, K.; Lin, K.-Q.; Huber, R.; Malic, E.; Höfer, U. Momentum-Resolved Observation of Exciton Formation Dynamics in Monolayer WS_2. *Nano Lett.* **2021**, *21* (13), 5867−5873.

(115) Madéo, J.; Man, M. K. L.; Sahoo, C.; Campbell, M.; Pareek, V.; Wong, E. L.; Al-Mahboob, A.; Chan, N. S.; Karmakar, A.; Mariserla, B. M. K.; Li, X.; Heinz, T. F.; Cao, T.; Dani, K. M. Directly Visualizing the Momentum-Forbidden Dark Excitons and Their Dynamics in Atomically Thin Semiconductors. *Science* **2020**, *370* (6521), 1199−1204.

(116) Yuan, L.; Huang, L. Exciton Dynamics and Annihilation in WS_2 2D Semiconductors. *Nanoscale* **2015**, *7* (16), 7402−7408.

(117) Sun, D.; Rao, Y.; Reider, G. A.; Chen, G.; You, Y.; Brézin, L.; Harutyunyan, A. R.; Heinz, T. F. Observation of Rapid Exciton−Exciton Annihilation in Monolayer Molybdenum Disulfide. *Nano Lett.* **2014**, *14* (10), 5625−5629.

(118) Poellmann, C.; Steinleitner, P.; Leierseder, U.; Nagler, P.; Plechinger, G.; Porer, M.; Bratschitsch, R.; Schuller, C.; Korn, T.; Huber, R. Resonant Internal Quantum Transitions and Femtosecond Radiative Decay of Excitons in Monolayer WSe_2. *Nat. Mater.* **2015**, *14* (9), 889−893.

(119) Rasmussen, F. A.; Thygesen, K. S. Computational 2D Materials Database: Electronic Structure of Transition-Metal Dichalcogenides and Oxides. *J. Phys. Chem. C* **2015**, *119* (23), 13169−13183.

(120) Xuan, F.; Quek, S. Y. Valley Zeeman Effect and Landau Levels in Two-Dimensional Transition Metal Dichalcogenides. *Phys. Rev. Res.* **2020**, *2* (3), 033256.

(121) Mouri, S.; Miyauchi, Y.; Toh, M.; Zhao, W.; Eda, G.; Matsuda, K. Nonlinear Photoluminescence in Atomically Thin Layered WSe_2 Arising from Diffusion-Assisted Exciton-Exciton Annihilation. *Phys. Rev. B* **2014**, *90* (15), No. 155449.

(122) Kumar, N.; Cui, Q.; Ceballos, F.; He, D.; Wang, Y.; Zhao, H. Exciton-Exciton Annihilation in $MoSe_2$ Monolayers. *Phys. Rev. B* **2014**, *89* (12), No. 125427.

(123) Raja, A.; Selig, M.; Berghäuser, G.; Yu, J.; Hill, H. M.; Rigosi, A. F.; Brus, L. E.; Knorr, A.; Heinz, T. F.; Malic, E.; Chernikov, A. Enhancement of Exciton−Phonon Scattering from Monolayer to Bilayer WS_2. *Nano Lett.* **2018**, *18* (10), 6135−6143.

(124) Demtröder, W. *Laser Spectroscopy*, 4th ed.; Springer-Verlag: 2008; Vol. *1*.

(125) Moody, G.; Kavir Dass, C.; Hao, K.; Chen, C.-H.; Li, L.-J.; Singh, A.; Tran, K.; Clark, G.; Xu, X.; Berghäuser, G.; Malic, E.; Knorr, A.; Li, X. Intrinsic Homogeneous Linewidth and Broadening Mechanisms of Excitons in Monolayer Transition Metal Dichalcogenides. *Nat. Commun.* **2015**, *6* (1), 8315.

(126) Bertoni, R.; Nicholson, C. W.; Waldecker, L.; Hübener, H.; Monney, C.; De Giovannini, U.; Puppin, M.; Hoesch, M.; Springate, E.; Chapman, R. T.; et al. Generation and Evolution of Spin-, Valley-, and Layer-Polarized Excited Carriers in Inversion-Symmetric WSe_2. *Phys. Rev. Lett.* **2016**, *117* (27), 277201.

(127) Beal, A. R.; Knights, J. C.; Liang, W. Y. Transmission Spectra of Some Transition Metal Dichalcogenides. II. Group Via: Trigonal Prismatic Coordination. *J. Phys. C: Solid State Phys.* **1972**, *5* (24), 3540−3551.

(128) Komsa, H.-P.; Krasheninnikov, A. V. Effects of Confinement and Environment on the Electronic Structure and Exciton Binding Energy of MoS_2 from First Principles. *Phys. Rev. B* **2012**, *86* (24), No. 241201.

(129) Moser, S. An Experimentalist's Guide to the Matrix Element in Angle Resolved Photoemission. *J. Electron Spectrosc. Relat. Phenom.* **2017**, *214*, 29−52.

(130) He, K. L.; Kumar, N.; Zhao, L.; Wang, Z. F.; Mak, K. F.; Zhao, H.; Shan, J. Tightly Bound Excitons in Monolayer WSe_2. *Phys. Rev. Lett.* **2014**, *113* (2), 026803.

(131) Bian, A.; He, D. W.; Hao, S. C.; Fu, Y.; Zhang, L.; He, J. Q.; Wang, Y. S.; Zhao, H. Dynamics of Charge-Transfer Excitons in a Transition Metal Dichalcogenide Heterostructure. *Nanoscale* **2020**, *12* (15), 8485−8492.

(132) Li, M.-Y.; Shi, Y.-M.; Cheng, C.-C.; Lu, L.-S.; Lin, Y.-C.; Tang, H. L.; Tsai, M.-L.; Chu, C.-W.; Wei, K.-H.; He, J.-H.; Chang, W.-H.; Suenaga, K.; Li, L.-J. Epitaxial Growth of a Monolayer WSe_2-MoS_2 Lateral p-n Junction with an Atomically Sharp. *Interface. Science* **2015**, *349* (6247), 524−528.

(133) Kilina, S. V.; Neukirch, A. J.; Habenicht, B. F.; Kilin, D. S.; Prezhdo, O. V. Quantum Zeno Effect Rationalizes the Phonon Bottleneck in Semiconductor Quantum Dots. *Phys. Rev. Lett.* **2013**, *110* (18), 180404.

(134) Craig, C. F.; Duncan, W. R.; Prezhdo, O. V. Trajectory Surface Hopping in the Time-Dependent Kohn-Sham Approach for Electron-Nuclear Dynamics. *Phys. Rev. Lett.* **2005**, *95* (16), 163001.

(135) Grundmann, M. *The Physics of Semiconductors*, 3rd ed.; Springer-Verlag: 2015.

(136) Li, Y.; Cui, Q.; Ceballos, F.; Lane, S. D.; Qi, Z.; Zhao, H. Ultrafast Interlayer Electron Transfer in Incommensurate Transition Metal Dichalcogenide Homobilayers. *Nano Lett.* **2017**, *17* (11), 6661−6666.

(137) He, J.; Kumar, N.; Bellus, M. Z.; Chiu, H.-Y.; He, D.; Wang, Y.; Zhao, H. Electron Transfer and Coupling in Graphene−Tungsten Disulfide Van Der Waals Heterostructures. *Nat. Commun.* **2014**, *5* (1), 5622.

(138) Lo, S.-Z. A.; Wang, L.; Loh, Z.-H. Pulse Propagation in Hollow-Core Fiber at High-Pressure Regime: Application to Compression of Tens of μJ Pulses and Determination of Nonlinear Refractive Index of Xenon at 1.03μm. *Appl. Opt.* **2018**, *57* (16), 4659−4664.

(139) Aeschlimann, M.; Brixner, T.; Fischer, A.; Kramer, C.; Melchior, P.; Pfeiffer, W.; Schneider, C.; Strüber, C.; Tuchscherer, P.; Voronine, D. V. Coherent Two-Dimensional Nanoscopy. *Science* **2011**, *333* (6050), 1723−1726.

(140) Liang, Y.; Li, B.-H.; Li, Z.; Zhang, G.; Sun, J.; Zhou, C.; Tao, Y.; Ye, Y.; Ren, Z.; Yang, X. Spatially Heterogeneous Ultrafast Interfacial Carrier Dynamics of 2D-MoS_2 Flakes. *Mater. Today Phys.* **2021**, *21*, 100506.

(141) Buckanie, N. M.; Göhre, J.; Zhou, P.; von der Linde, D.; Horn-von Hoegen, M.; Meyer zu Heringdorf, F. J. Space Charge Effects in Photoemission Electron Microscopy Using Amplified Femtosecond Laser Pulses. *J. Phys.: Condens. Matter* **2009**, *21* (31), 314003.

(142) Schönhense, B.; Medjanik, K.; Fedchenko, O.; Chernov, S.; Ellguth, M.; Vasilyev, D.; Oelsner, A.; Viefhaus, J.; Kutnyakhov, D.; Wurth, W.; Elmers, H. J.; Schönhense, G. Multidimensional Photo-emission Spectroscopy—the Space-Charge Limit. *New J. Phys.* **2018**, *20* (3), 033004.

(143) Kresse, G.; Hafner, J. Ab Initio Molecular Dynamics for Liquid Metals. *Phys. Rev. B* **1993**, *47* (1), 558−561.

(144) Kresse, G.; Furthmüller, J. Efficient Iterative Schemes for Ab Initio Total-Energy Calculations Using a Plane-Wave Basis Set. *Phys. Rev. B* **1996**, *54* (16), 11169−11186.

(145) Ernzerhof, M.; Scuseria, G. E. Assessment of the Perdew−Burke−Ernzerhof Exchange-Correlation Functional. *J. Chem. Phys.* **1999**, *110* (11), 5029−5036.

(146) Kresse, G.; Joubert, D. From Ultrasoft Pseudopotentials to the Projector Augmented-Wave Method. *Phys. Rev. B* **1999**, *59* (3), 1758−1775.

(147) Grimme, S.; Antony, J.; Ehrlich, S.; Krieg, H. A Consistent and Accurate Ab Initio Parametrization of Density Functional Dispersion Correction (DFT-D) for the 94 Elements H-Pu. *J. Chem. Phys.* **2010**, *132* (15), 154104.

(148) Tully, J. C. Molecular Dynamics with Electronic Transitions. *J. Chem. Phys.* **1990**, *93* (2), 1061−1071.

(149) Fischer, S. A.; Habenicht, B. F.; Madrid, A. B.; Duncan, W. R.; Prezhdo, O. V. Regarding the Validity of the Time-Dependent Kohn−Sham Approach for Electron-Nuclear Dynamics Via Trajectory Surface Hopping. *J. Chem. Phys.* **2011**, *134* (2), 024102.

(150) Jaeger, H. M.; Fischer, S.; Prezhdo, O. V. Decoherence-Induced Surface Hopping. *J. Chem. Phys.* **2012**, *137* (22), 22A545.

(151) Akimov, A. V.; Prezhdo, O. V. Persistent Electronic Coherence Despite Rapid Loss of Electron−Nuclear Correlation. *J. Phys. Chem. Lett.* **2013**, *4* (22), 3857−3864.

(152) Silbey, R. J. Principles of Nonlinear Optical Spectroscopy by Shaul Mukamel (University of Rochester). Oxford University Press: New York. 1995. Xviii + 543 Pp. $65.00. Isbn 0−19−509278−3. *J. Am. Chem. Soc.* **1996**, *118* (50), 12872−12872.

(153) Akimov, A. V.; Prezhdo, O. V. The PYXAID Program for Non-Adiabatic Molecular Dynamics in Condensed Matter Systems. *J. Chem. Theory Comput.* **2013**, *9* (11), 4959−4972.

(154) Akimov, A. V.; Prezhdo, O. V. Advanced Capabilities of the PYXAID Program: Integration Schemes, Decoherence Effects, Multi-excitonic States, and Field-Matter Interaction. *J. Chem. Theory Comput.* **2014**, *10* (2), 789−804.

(155) Neukirch, A. J.; Hyeon-Deuk, K.; Prezhdo, O. V. Time-Domain Ab Initio Modeling of Excitation Dynamics in Quantum Dots. *Coord. Chem. Rev.* **2014**, *263*, 161−181.

(156) Chu, W. B.; Saidi, W. A.; Prezhdo, O. V. Long-Lived Hot Electron in a Metallic Particle for Plasmonics and Catalysis: Ab Initio Nonadiabatic Molecular Dynamics with Machine Learning. *ACS Nano* **2020**, *14* (8), 10608−10615.

(157) Sarkar, R.; Kar, M.; Habib, M.; Zhou, G. Q.; Frauenheim, T.; Sarkar, P.; Pal, S.; Prezhdo, O. V. Common Defects Accelerate Charge Separation and Reduce Recombination in Cnt/Molecule Composites: Atomistic Quantum Dynamics. *J. Am. Chem. Soc.* **2021**, *143* (17), 6649−6656.

(158) Li, W.; She, Y. L.; Vasenko, A. S.; Prezhdo, O. V. Ab Initio Nonadiabatic Molecular Dynamics of Charge Carriers in Metal Halide Perovskites. *Nanoscale* **2021**, *13* (23), 10239−10265.

(159) Tomko, J. A.; Runnerstrom, E. L.; Wang, Y. S.; Chu, W. B.; Nolen, J. R.; Olson, D. H.; Kelley, K. P.; Cleri, A.; Nordlander, J.; Caldwell, J. D.; Prezhdo, O. V.; Maria, J. P.; Hopkins, P. E. Long-Lived Modulation of Plasmonic Absorption by Ballistic Thermal Injection. *Nat. Nanotechnol.* **2021**, *16* (1), 47−51.

(160) Zhang, L. L.; Chu, W. B.; Zhao, C. Y.; Zheng, Q. J.; Prezhdo, O. V.; Zhao, J. Dynamics of Photoexcited Small Polarons in Transition-Metal Oxides. *J. Phys. Chem. Lett.* **2021**, *12* (9), 2191−2198.

(161) Li, H.; Contryman, A. W.; Qian, X.; Ardakani, S. M.; Gong, Y.; Wang, X.; Weisse, J. M.; Lee, C. H.; Zhao, J.; Ajayan, P. M.; Li, J.; Manoharan, H. C.; Zheng, X. Optoelectronic Crystal of Artificial Atoms in Strain-Textured Molybdenum Disulphide. *Nat. Commun.* **2015**, *6* (1), 7381.